Accepted Manuscript

Topology optimization for auxetic metamaterials based on isogeometric analysis

Jie Gao, Huipeng Xue, Liang Gao, Zhen Luo

PII: S0045-7825(19)30224-5
DOI: https://doi.org/10.1016/j.cma.2019.04.021
Reference: CMA 12409

To appear in: *Comput. Methods Appl. Mech. Engrg.*

Received date : 10 January 2019
Revised date : 15 March 2019
Accepted date : 16 April 2019

Please cite this article as: J. Gao, H. Xue, L. Gao et al., Topology optimization for auxetic metamaterials based on isogeometric analysis, *Computer Methods in Applied Mechanics and Engineering* (2019), https://doi.org/10.1016/j.cma.2019.04.021

Highlights (for review)

Highlights:

- A more efficient and effective isogeometric topology optimization (ITO) method for the systematic design of auxetic metamaterials is developed.
- The IGA-based TO offers many positive features for the optimization of auxetic metamaterials, which might be firstly studied in the current work.
- A series of new and interesting 3D auxetic metamaterials are presented in the current work.

Topology optimization for auxetic metamaterials based on isogeometric analysis

Jie Gao[1, 2], Huipeng Xue[1], Liang Gao[2], †Zhen Luo[1]

[1]*The School of Mechanical and Mechatronic Engineering, University of Technology Sydney, 15 Broadway, Ultimo, NSW 2007, Australia*

[2]*The State Key Lab of Digital Manufacturing Equipment and Technology, Huazhong University of Science and Technology, 1037 Luoyu Road, Wuhan, Hubei 430074, China*

†***Corresponding author:*** *Tel.:* +61-2-95142994; *E-mail:* zhen.luo@uts.edu.au *(Dr/Prof Z. Luo)*

Abstract

In this paper, an effective and efficient topology optimization method, termed as Isogeometric Topology Optimization (ITO), is proposed for systematic design of both 2D and 3D auxetic metamaterials based on isogeometric analysis (IGA). Firstly, a density distribution function (DDF) with the desired smoothness and continuity, to represent the topological changes of structures, is constructed using the Shepard function and non-uniform rational B-splines (NURBS) basis functions. Secondly, an energy-based homogenization method (EBHM) to evaluate material effective properties is numerically implemented by IGA, with the imposing of the periodic boundary formulation on material microstructure. Thirdly, a topology optimization formulation for 2D and 3D auxetic metamaterials is developed based on the DDF, where the objective function is defined as a combination of the homogenized elastic tensor and the IGA is applied to solve the structural responses. A relaxed optimality criteria (OC) method is used to update the design variables, due to the non-monotonic property of the problem. Finally, several numerical examples are used to demonstrate the effectiveness and efficiency of the proposed method. A series of auxetic microstructures with different deformation mechanisms (e.g. the re-entrant and chiral) can be obtained. The auxetic behavior of material microstructures are numerically validated using ANSYS, and the optimized designs are prototyped using the Selective Laser Sintering (SLS) technique.

Keywords. Auxetic metamaterials; Topology optimization; Isogeometric analysis; Homogenization.

1 Introduction

Auxetic metamaterials are rationally artificial materials [1] with the Negative Poisson's Ratio (NPR), which exhibit the counterintuitive dilatational behavior, expanding laterally if stretched and contracting laterally when compressed. Since they were firstly found in foam structures [2], auxetic metamaterials have gained a wide range of applications in engineering, due to their enhanced shear resistance, indentation resistance, fracture toughness and etc [3]. It is known that the effective properties of auxetics are mainly dependent on the architecture of the microstructure that are periodically distributed in the bulk material, rather than the constituent properties of the base material. Hence, many works have tried to achieve artificial materials with NPRs by adjusting the geometric configuration of material microstructures, such as the re-entrant structures [4,5], chiral auxetics [6,7], and rotating-type structures [8]. A comprehensive review for different types of auxetics can refer to [9,10].

In recent years, topology optimization has made remarkable progress in architecting materials with new properties [11,12]. Topology optimization is a numerically iterative procedure to optimize the distribution of materials in a given design domain, subject to a specified objective function and constraint(s) [13]. Several topology optimization methods have been developed, such as the homogenization method [14], the solid isotropic material with penalization (SIMP) method [15,16], the evolutionary structural optimization (ESO) method [17] and the level set method (LSM) [18–20] and so on. Topology optimization methods has been combined with the homogenization method [21] to optimize the architecture of microstructures [22–24] with tailored effective properties, and even more advanced topological designs [25–27].

There have been several works for the optimization of material microstructures with the auxetic behavior, e.g. [28–35]. In [24,30,34], the nonlinear properties were also considered in the optimization of material microstructures with the programmable Poisson's ratios, and a subsequent shape optimization was applied to achieve any given Poisson's ratio in 3D auxetic microstructures [34]. Zong et al [35] developed a two-step design process for microstructures with the desired Poisson's ratios, where the material optimization method was firstly used to generate a preliminary solution and then the boundary evolvement optimization was applied to refine the quality of the structural surfaces for the manufacturing. The parametric level set method was also used to optimize auxetic microstructures [29]. The polygonal finite elements were used in the topology optimization of auxetic structures using compliant mechanisms [36]. Topology optimization has been applied to implement 3D auxetic microstructures, but it still keeps challenging when the iterative efficiency comes into the picture. For instance, in [28], a highly dense finite element mesh (100^3) to ensure the numerical precision was employed in the optimization of 3D material microstructures with the auxetic behavior, but with a large number of iterations (overall 3000), which might limit the further applications of most conventional topology optimization methods in finding novel material microstructures. An alternative strategy, that the geometric symmetries are pre-imposed on material microstructures, is discussed to reduce the design freedoms to a great extent [34,35]. However, the reduced design space might lower the possibility to search for the novel auxetic microstructures. Hence, a more effective and efficient topology optimization method for designing 3D auxetic metamaterials is still in demand.

In topology optimization problems, the finite element method (FEM) [37] has been employed dominantly to perform the numerical analysis. The FEM is also one factor to influence the effectiveness of the topology optimization for the design of auxetic microstructures, particularly the 3D scenario. This is because: (1) The finite element mesh is just an approximation of the original shape of the design domain, which lowers the numerical accuracy; (2) The lower-order (C0) continuity of the responses between the neighboring finite elements, even if the higher-order finite elements are utilized; (3) The lower efficiency to achieve a finite element mesh with the high quality. Recently, the isogeometric analysis (IGA) [38,39] has attracted much interests, due to its favorable features in numerical analysis, such as the consistency between the computer-aided design (CAD) model and the computer-aided engineering (CAE) model, and the high-order continuity between different elements [40].

Recently, IGA has been applied to the topology optimization problems, such as the earlier work [41] that used the trimmed spline surface. Later, an isogeometric topology optimization approach was proposed in [42], where the Optimality Criteria (OC) algorithm was used to evolve the design variables. In [43], a phase field model was also combined with the IGA for topology optimization of continuum structures, where the exact representation of the geometry in IGA was suitable for the phase field model. Qian [44] constructed the B-spline space with the intrinsic filter for the topology optimization. After that, a parametric level set method [45] with IGA was studied, where the level set function was interpolated by NURBS basis functions [46], rather than the compactly supported radial basis functions. The LSM combined with IGA was also discussed in the topology optimization considering stress problems [47] and flexoelectric materials [48]. A global stress constraint was also studied in an IGA-based SIMP framework [49]. In [50], R-functions and an collocation scheme was employed to develop the IGA-based Moving Morphable Components method [51]. Moreover, the multi-resolution topology optimization problem was discussed in an IGA-based SIMP framework [52], and the similar topology optimization formulation was used to optimize the multi-material structures [53]. As we can see, most of the existed works using IGA are only performed for the macro-scale topology optimization problems. Although the IGA-based shape optimization has already been studied in the applications of the smoothed petal auxetic structures [54], how to develop an IGA-based topology optimization framework for the design of 2D and 3D auxetic metamaterials is still a challenging topic in the research field of structural optimization.

The current work is motivated to develop a more effective and efficient isogeometric topology optimization (ITO) method for the optimization of auxetic metamaterials, particularly 3D material microstructures. In the proposed ITO method, a DDF with the sufficient smoothness and continuity is firstly constructed to represent the evolving of the structural topology, where the Shepard function is employed to enhance the overall smoothness of the nodal densities at the control points and the NURBS basis functions control the continuity of the DDF. Later, an IGA-based EBHM is numerically implemented to evaluate material effective properties, with the imposing of the periodic boundary formulation on material microstructure. Finally, an ITO formulation for both 2D and 3D auxetic metamaterials is developed using the DDF, and a combination of the homogenized elastic tensor is expressed as the objective function. Hence, the current topology optimization formulation aims to optimize the densities of the DDF with desired smoothness and continuity to guarantee 2D and 3D material microstructures with expected auxetic behavior, rather than finding spatial arrangements of finite elements as done in many previous works.

2 NURBS-based IGA

In IGA [38,39], a unified mathematical form is developed using the same NURBS basis functions for the CAD and CAE models to keep the consistency of them.

2.1 NURBS

An example of a square modelled by NURBS is shown in **Fig. 1**. The NURBS basis functions are linearly combined with a series of control points plotted with the red color to construct the geometrical model shown in **Fig. 1** (*b*), and the mathematical form of the NURBS surface $\mathbf{S}(\xi,\eta)$ is given as:

$$\mathbf{S}(\xi,\eta)=\sum_{i=1}^{n}\sum_{j=1}^{m}R_{i,j}^{p,q}(\xi,\eta)\mathbf{P}_{i,j} \tag{1}$$

where n and m are the numbers of control points in two parametric directions, and ξ and η denote the corresponding parametric directions. p and q are the polynomial orders. The detailed information for the square is listed below **Fig. 1**. $\mathbf{P}_{i,j}$ correspond to the $(i,j)_{th}$ control point. It should be noted that control points are not necessarily on the structural design domain. R are the bivariate NURBS basis functions, and which are constructed by the B-spline basis functions as:

$$R_{i,j}^{p,q}(\xi,\eta)=\frac{N_{i,p}(\xi)M_{j,q}(\eta)\omega_{ij}}{\sum_{\hat{i}=1}^{n}\sum_{\hat{j}=1}^{m}N_{\hat{i},p}(\xi)M_{\hat{j},q}(\eta)\omega_{\hat{i}\hat{j}}} \tag{2}$$

where ω_{ij} is the positive weight for the $(i,j)_{th}$ control point $\mathbf{P}_{i,j}$. $N_{i,p}$ and $M_{j,q}$ are the univariate B-spline basis functions in two parametric directions, respectively. The B-spline basis function is defined by the Cox-de-Boor formula [55], and the recursive formula in ξ direction with a non-decreasing knot vector $\Xi=\{\xi_1,\xi_2,\cdots,\xi_{n+p+1}\}$ is defined as:

$$\begin{cases} N_{i,0}(\xi)=\begin{cases}1 & if\ \xi_i\le\xi_{i+1}\\ 0 & otherwise\end{cases}, & p=0\\ N_{i,p}(\xi)=\dfrac{\xi-\xi_i}{\xi_{i+p}-\xi_i}N_{i,p-1}(\xi)+\dfrac{\xi_{i+p+1}-\xi}{\xi_{i+p+1}-\xi_{i+1}}N_{i+1,p-1}(\xi), & p\ge 1\end{cases} \tag{3}$$

It is noted that the fractions with the form 0/0 in Eq. (3) are defined as zero. Similarly, the basis functions $M_{j,q}$ in the η direction are also defined by Eq. (3) with the knot vector. The NURBS basis functions of the square in two parametric directions are respectively displayed in **Fig. 1** (*d*) and (*e*). The bivariate basis functions are also plotted in **Fig. 1** (*f*). we can easily see that the NURBS basis functions are featured with several important properties: (1) **Nonnegativity**: $N_{i,p}(\xi)\ge 0$; (2) **Local support**: the support of each basis function $N_{i,p}$ is contained in the interval $[\xi_i, \xi_{i+p+1}]$; (3) **Partition of unity**: for an arbitrary knot span $[\xi_i, \xi_{i+1}]$, $\forall\xi \in [\xi_i, \xi_{i+1}]$, $\sum_{j=i-p}^{i} N_{j,p}(\xi) = 1$; (4) **Continuity**: The continuity between knot spans is equal to C^{p-k} where k is the multiplicity of the knots [38,39].

As we can see, the CAD model with a series of control points shown in **Fig. 1** (*b*) and the CAE model with an array of discretized elements displayed in **Fig. 1** (*c*) are consistent. The final integrated form is illustrated in **Fig. 1** (*g*). We should note that the current work just provides a simple illustration of the square. Even if the curved structures are considered, the corresponding CAD and CAE models can be still kept in a unified form, and the IGA mesh is consistent with the structural domain. By virtue of the important properties of NURBS basis functions, NURBS can be featured with the **strong convex hull property**, **differentiability**, **local modification** and **variation diminishing property** [38,39].

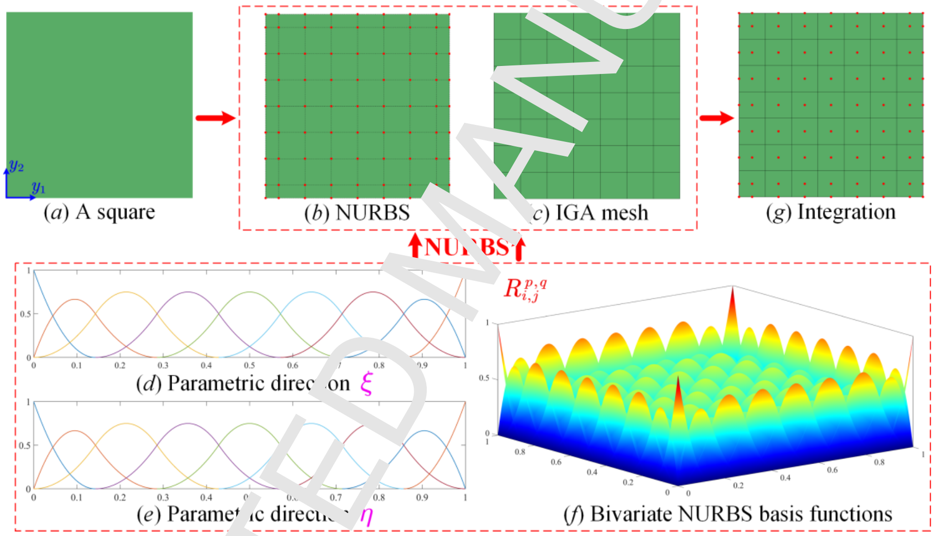

Fig. 1. NURBS-based IGA for a square: $\Xi = \{0,0,0,0.1429,\cdots,0.8517,1,1,1\}$, $\mathcal{H} = \{0,0,0,0.1429,\cdots,0.8517,1,1,1\}$; $n = m = 9$; $p = q = 2$.

2.2 Numerical discretization in the IGA

The NURBS basis functions are firstly applied to parametrize the structural domain, and then construct the space for structural responses. As far as the latter, the key principle is that the continuous solution space is approximately defined by a linear combination of all NURBS basis functions with the nodal responses on control points. The mathematical formula of the space keeps the same as the geometrical model in Eq. (1), while control coefficients correspond to the structural responses on control points, expressed as:

$$\mathbf{x}(\xi,\eta) = \sum_{i=1}^{n}\sum_{j=1}^{m} R_{i,j}^{p,q}(\xi,\eta)\mathbf{x}_{i,j} \tag{4}$$

where $\mathbf{x}$ is the field of structural responses in design domain, and $\mathbf{x}_{i,j}$ is the structural response on the control point $(i,j)_{th}$.

Considering the linearly elastic structures in IGA, the system stiffness matrix is obtained by assembling the element stiffness matrix which is calculated by the Gauss quadrature method [38,39] given as:

$$\mathbf{K}_e = \sum_{i=1}^{3}\sum_{j=1}^{3}\{\mathbf{B}^T(\xi_i,\eta_j)\mathbf{D}\mathbf{B}(\xi_i,\eta_j)|\boldsymbol{J}_1(\xi_i,\eta_j)||\boldsymbol{J}_2(\xi_i,\eta_j)|\omega_i\omega_j\} \tag{5}$$

where $\mathbf{B}$ is the strain-displacement matrix calculated by the partial derivatives of NURBS basis functions with respect to parametric coordinates. In the iso-parametric formulation, two mappings have to be defined: (1) $\mathbf{X}: \widehat{\Omega}_e \rightarrow \Omega_e$ denotes the parametric space mapping into the physical space; (2) $\mathbf{Y}: \widetilde{\Omega}_e \rightarrow \widehat{\Omega}_e$ maps the bi-unit parent element into the parametric element, as shown in **Fig. 2**. $\boldsymbol{J}_1$ and $\boldsymbol{J}_2$ are the Jacobi matrices of two mappings, respectively. All Gauss quadrature points in the IGA mesh and 3×3 Gauss quadrature points in an IGA element are shown in **Fig. 2**. (ξ_i,η_j) is the parametric coordinate of the Gauss quadrature point, and ω_i *and* ω_j are the corresponding quadrature weights.

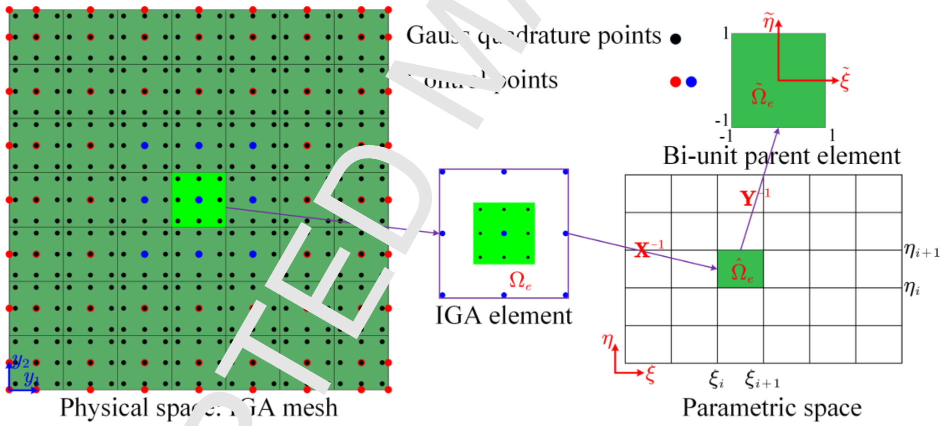

Fig. 2. IGA mesh with Gauss quadrature points

In a conclusion, NURBS basis functions are firstly applied to parametrize the structural domain, and then discretize it into a series of IGA elements, as well as serving as the basis functions to construct the solution space. Hence, the NURBS basis functions unify geometry construction, spatial discretization and numerical analysis into a single framework.

3 IGA-based EBHM

The principle of the homogenization is that the macroscopic effective properties of the bulk material are determined by using the information from the microstructure [21]. There are two basic requirements to be maintained in the homogenization: (1) the scales of the material microstructure are much smaller than that of the bulk material, and (2) material microstructure needs to be periodically distributed in the bulk material. An example of the bulk material with only a kind of material microstructure is shown in **Fig. 3**, where the microstructure is described in the coordinate system **y**.

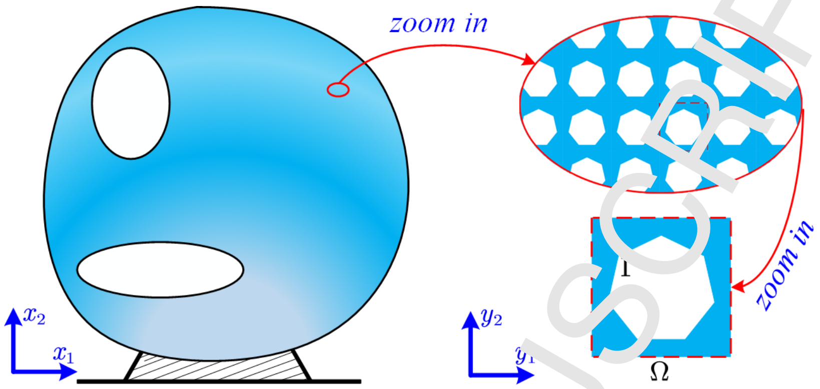

(a) The bulk material (b) Material microstructure

Fig. 3. The bulk material composed of a kind of material microstructure

Considering the linear elasticity, the displacement field $\mathbf{u}^{\epsilon}$ at the bulk material can be characterized by the asymptotic expansion theory, expressed as:

$$\mathbf{u}^{\epsilon}(\mathbf{x}) = \mathbf{u}_0(\mathbf{x},\mathbf{y}) + \epsilon\mathbf{u}_1(\mathbf{x},\mathbf{y}) + \epsilon^2\mathbf{u}_2(\mathbf{x},\mathbf{y}) + \cdots \tag{6}$$

where ϵ is the aspect ratio between the scales of the microstructure and the bulk material, which is far less than 1. For numerical simplicity, only the first-order variation term with respect to the parameter expansion ϵ is considered. The effective elastic tensor of the bulk material D^H_{ijkl} can be computed as:

$$D^H_{ijkl} = \frac{1}{|\Omega|}\int_{\Omega}\left(\varepsilon^{0(ij)}_{pq} - \varepsilon_{pq}\left(u^{ij}\right)\right) D_{pqrs}\left(\varepsilon^{0(kl)}_{rs} - \varepsilon_{rs}\left(u^{kl}\right)\right) d\Omega \tag{7}$$

where $|\Omega|$ is the area (2D) or volume (3D) of the microstructure, and D_{pqrs} is the locally varying elastic property. $\varepsilon^{0(ij)}_{pq}$ is the linearly independent unit test strain field, containing three components in 2D and six in 3D. $\varepsilon_{pq}\left(u^{ij}\right)$ denotes the unknown strain field in the microstructure, which is solved by the following linear elasticity equilibrium equation with **y**-periodic boundary conditions (PBCs):

$$\int_{\Omega}\varepsilon_{pq}\left(u^{ij}\right)D_{pqrs}\varepsilon_{rs}\left(\delta u^{ij}\right) d\Omega = \int_{\Omega}\varepsilon^{0(ij)}_{pq}D_{pqrs}\varepsilon_{rs}\left(\delta u^{ij}\right) d\Omega, \quad \forall \delta u \in H_{per}(\Omega, \mathbb{R}^d) \tag{8}$$

where δu is the virtual displacement in the microstructure belonging to the admissible displacement space H_{per} with **y**-periodicity, and d denotes the dimension of material microstructure.

The homogenization is numerically performed by discretizing and solving Eq. (8) using the finite element method (FEM), namely numerical homogenization [56], and the utmost importance is the imposing of the PBCs on the microstructure. As an alternative method, the EBHM with a simplified periodic boundary formulation [22,32,57] is developed. Here, the numerical analysis of material microstructure is performed by IGA, with the imposing of the periodic boundary formulation in the EBHM. In IGA, the displacement field in material microstructure is approximately expressed by a combination of the NURBS basis functions with the displacements at control points:

$$\mathbf{u} = \sum_{i=1}^{n} \sum_{j=1}^{m} R_{i,j}^{p,q}(\xi, \eta) \mathbf{u}_{i,j} \tag{9}$$

where $\mathbf{u}_{i,j}$ denote the displacements of the $(i,j)_{th}$ control point. As we can see, NURBS basis functions are linearly combined with nodal displacements to approximate the displacement field in the microstructure. In the application of the EBHM to evaluate material effective properties, the displacement field in material microstructure needs to satisfy the PBCs, and a general form is expressed as:

$$\mathbf{u}_k^+ - \mathbf{u}_k^- = \varepsilon(\mathbf{u}_0)\Delta k \tag{10}$$

where k denote the normal direction of the structural boundary. $\mathbf{u}_k^+$ indicate the displacements of points at the structural boundary with the normal direction k, and the normal direction is in the positive direction of the coordinate axis. $\mathbf{u}_k^-$ correspond to the displacements of points at the opposite structural boundary. Δk is the scale of the material microstructure along the direction of k. The expressions of the boundary constraint equations in PBCs in detail can refer to [32] for 2D and [57] for 3D.

4 Isogeometric topology optimization (ITO)

As already pointed out in Section 2, the physical coordinates of control points act as control coefficients of Eq. (1) in parametrizing of the structural geometry. If each control point is assigned to a nodal density, the NURBS response will correspond to a field of density in the structural domain, namely density distribution function (DDF). The topology optimization formulation to achieve auxetic metamaterials can be developed using the DDF, where IGA is applied to solve structural responses in material microstructure. It is important to notice that NURBS basis functions bridge the geometrical model, numerical analysis model, DDF and topology optimization formulation.

4.1 Density distribution function (DDF)

Before developing the DDF, the definition of nodal densities assigned to control points needs to satisfy two basic conditions [58–61]: (1) non-negativity; and (2) the strict bounds ranging from 0 to 1. Meanwhile, the Shepard function is firstly used to improve the overall smoothness of nodal densities, so as to make sure the smoothness of the DDF. The corresponding mathematical model is given as:

$$\mathcal{G}(\rho_{i,j}) = \sum_{i=1}^{\mathcal{N}} \sum_{j=1}^{\mathcal{M}} \psi(\rho_{i,j}) \rho_{i,j} \tag{11}$$

where $\mathcal{G}(\rho_{i,j})$ is the smoothed nodal density assigned to the $(i,j)_{th}$ control point, and $\rho_{i,j}$ is the initial nodal density. $\mathcal{N}$ and $\mathcal{M}$ are the numbers of nodal densities located at the local support area of the current nodal density in two parametric directions respectively, as shown in the sub area bounded by the blue circle in **Fig. 4**. Hence, the key idea of the current smoothing scheme for nodal densities is that each nodal density is equal to the mean value of all nodal densities in the local area of the current nodal density. $\psi(\rho_{i,j})$ is the Shepard function [62] of the $(i,j)_{th}$ nodal density, given as:

$$\psi(\rho_{i,j}) = \frac{w(\rho_{i,j})}{\sum_{\hat{i}=1}^{\mathcal{N}} \sum_{\hat{j}=1}^{\mathcal{M}} w(\rho_{\hat{i},\hat{j}})} \tag{12}$$

where w is the weight function of the nodal density of the $(i,j)_{th}$ control point, and the weight function can be constructed by many functions, such as the inverse distance weighting function, exponential cubic spline, quartic spline functions and radial basis functions (RBFs) [60,61]. The compactly supported RBFs (CSRBFs) with the C^4 continuity [63] are employed in this work due to the compactly supported, the high-order continuity and the nonnegativity over the local domain, by:

$$w(r) = (1-r)_+^6 (35r^2 + 18r + 3) \tag{13}$$

where $r = d/d_m$, and d is the Euclidean distance between the current nodal density and the other nodal density in the support domain. d_m is the radius of this domain shown in **Fig. 4**. It can be obtained that the smoothed nodal densities can still maintain the necessary conditions for a physically meaningful material density [58–61]. It is important to notice that the Shepard function to smooth the nodal densities is not just a processing procedure, and it will be also considered in the next topology optimization formulation.

Assuming that the DDF in the structural domain is denoted by $\mathcal{X}$, the DDF is constructed by the NURBS basis functions with a linear combination of the smoothed nodal densities, expressed as:

$$\mathcal{X}(\xi,\eta) = \sum_{i=1}^{n} \sum_{j=1}^{m} R_{i,j}^{p,q}(\xi,\eta) \mathcal{G}(\rho_{i,j}) \tag{14}$$

It can be seen that Eq. (14) for the DDF has the same mathematical formula for NURBS in Eq. (1). The key difference is the physical meaning of control coefficients. The initial NURBS-based geometrical model for the domain has been converted into a representation of the DDF. Eq. (14) is the global form, which can be expanded as a local form depended on the local area of $(\xi,\eta) \in [\xi_i, \xi_{i+1}] \times [\eta_j, \eta_{j+1}]$, that

$$\mathcal{X}(\xi,\eta)=\sum_{e=i-p}^{i}\sum_{f=j-q}^{j}R_{e,f}^{p,q}(\xi,\eta)\mathcal{G}(\rho_{e,f}) \tag{15}$$

By virtue of the properties of NURBS described in Section 2.1, the current developed DDF is also featured with the non-negativity and strict-bounds. Hence, the DDF can guarantee the strict physical meaning of the material density for structural domain in the next optimization formulation. The non-interpolant of NURBS has no influence on the DDF, originating from that control points are not necessarily located at the structural domain. Moreover, the variation diminishing property of NURBS can make sure the non-oscillatory of the DDF, even if the higher-order NURBS basis functions are used [38,39]. Hence, the DDF with several merits can be beneficial to the latter topology optimization.

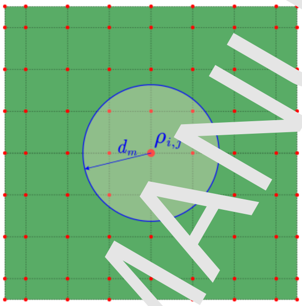

Fig. 4. Nodal densities assigned to control points

4.2 ITO formulation for auxetic metamaterials

The Poisson's ratio of materials is equal to the aspect ratio of the transverse contraction strain to longitudinal extension strain in the direction of stretching force. Considering the material elastic tensor, Poisson's ratios in two directions of 2D materials can be defined by $\upsilon_{12}=D_{1122}/D_{1111}$ and $\upsilon_{21}=D_{1122}/D_{2222}$. In order to generate materials with the NPR property, several different objective functions are developed, such as the minimization of the weighted square difference between the expected elastic tensor and the evaluated elastic tensor [28–30,35], the minimization of the difference between the predicted NPR and its target [33], minimizing the combination of the elastic tensor [25,32] and so on [34].

Here, the objective function of the optimization of auxetic metamaterials is expressed by a combination of the homogenized elastic tensor. It is known that the occurrence of the auxetic behavior is highly related to the rotating effect of mechanisms in material microstructures [22,25]. As defined in Eq. (16), minimizing the term $\sum_{\hat{i},\hat{j}=1,\hat{i}=\hat{j}}^{d}D_{\hat{i}\hat{i}\hat{j}\hat{j}}^{H}$ can guarantee the generation of the mechanism-type layouts, which is beneficial to facilitate microstructures with the auxetic behavior. Meanwhile, the term $\sum_{\hat{i},\hat{j}=1,\hat{i}\neq\hat{j}}^{d}D_{\hat{i}\hat{i}\hat{j}\hat{j}}^{H}$ can prevent mechanism-type topologies when its value is smaller than 0. In the defined optimization formulation, the optimizer tends to maximize the second term $\sum_{\hat{\imath},\hat{\jmath}=1,\hat{\imath}=\hat{\jmath}}^{d} D_{\hat{\imath}\hat{\imath}\hat{\jmath}\hat{\jmath}}^{H}$ and minimize the first term $\sum_{\hat{\imath},\hat{\jmath}=1,\hat{\imath}\neq\hat{\jmath}}^{d} D_{\hat{\imath}\hat{\imath}\hat{\jmath}\hat{\jmath}}^{H}$, simultaneously, so that the objective function can be gradually minimized and materials can be featured with the auxetic behavior in all directions.

$$\begin{cases} Find: \boldsymbol{\rho}\ \left\{\left[\rho_{i,j}\right]_{2D}\ \ \left[\rho_{i,j,k}\right]_{3D}\right\} \\ Min: J(\mathbf{u},\mathcal{X}) = \left\{\sum_{\hat{\imath},\hat{\jmath}=1,\hat{\imath}\neq\hat{\jmath}}^{d} D_{\hat{\imath}\hat{\imath}\hat{\jmath}\hat{\jmath}}^{H}(\mathbf{u},\mathcal{X})\right\} - \beta\left\{\sum_{\hat{\imath},\hat{\jmath}=1,\hat{\imath}=\hat{\jmath}}^{d} D_{\hat{\imath}\hat{\imath}\hat{\jmath}\hat{\jmath}}^{H}(\mathbf{u},\mathcal{X})\right\} \\ S.t: \begin{cases} G(\mathcal{X}) = \dfrac{1}{|\Omega|}\displaystyle\int_{\Omega} \mathcal{X}(\boldsymbol{\rho}) v_0 \, d\Omega - V_0 \leq 0 \\ a(\mathbf{u},\delta\mathbf{u}) = l(\delta\mathbf{u}), \qquad \forall\delta\mathbf{u} \in H_{per}(\Omega,\mathbb{R}^d) \\ 0 < \rho_{min} \leq \boldsymbol{\rho} \leq 1, (i = 1,2,\cdots,n; j = 1,2,\cdots,m; k = 1,2,\cdots,l) \end{cases} \end{cases} \tag{16}$$

where $\boldsymbol{\rho}$ denotes the nodal densities assigned to control points, working as the design variables. J is the objective function. β is a weighting parameter to denote the importance of the corresponding terms. d is the spatial dimension of materials. G is the volume constraint, in which V_0 is the maximum value and v_0 is the volume fraction of the solid. $\mathcal{X}$ is the DDF in Eq. (14). $\mathbf{u}$ is the unknown displacement field in material microstructure, which have to satisfy the PBCs given in Eq. (10). $\delta\mathbf{u}$ is the virtual displacement field belonging to the admissible displacement space H_{per} with $\mathbf{y}$-periodicity, which is calculated by the linearly elastic equilibrium equation. a and l are the bilinear energy and linear load functions, as:

$$\begin{cases} a(\mathbf{u},\delta\mathbf{u}) = \displaystyle\int_{\Omega} \boldsymbol{\varepsilon}(\mathbf{u})\left(\mathcal{X}(\boldsymbol{\rho})\right)^{\gamma}\mathbf{D_0}\boldsymbol{\varepsilon}(\delta\mathbf{u})\, d\Omega \\ l(\delta\mathbf{u}) = \displaystyle\int_{\Omega} \boldsymbol{\varepsilon}^{\mathbf{0}}\left(\mathcal{X}(\boldsymbol{\rho})\right)^{\gamma}\mathbf{D_0}\boldsymbol{\varepsilon}(\delta\mathbf{u})\, d\Omega \end{cases} \tag{17}$$

It should be noted that the elastic tensor is assumed to be an exponential function with respect to the DDF, and γ is the penalization parameter. $\mathbf{D_0}$ is the constitutive elastic tensor of the basic material.

4.3 Design Sensitivity Analysis

In Eq. (16), the ITO formulation for auxetics are developed using the DDF, and which is expressed by the linear combination of the nodal densities and NURBS basis functions. Moreover, the nodal densities are design variables. Hence, we firstly derive the first-order derivative of the objective function with respect to the DDF before obtaining the sensitivity analysis with respect to the design variables, as:

$$\frac{\partial J}{\partial \mathcal{X}} = \left\{\sum_{\hat{\imath},\hat{\jmath}=1,\hat{\imath}\neq\hat{\jmath}}^{d} \frac{\partial D_{\hat{\imath}\hat{\imath}\hat{\jmath}\hat{\jmath}}^{H}}{\partial \mathcal{X}}\right\} - \beta\left\{\sum_{\hat{\imath},\hat{\jmath}=1,\hat{\imath}=\hat{\jmath}}^{d} \frac{\partial D_{\hat{\imath}\hat{\imath}\hat{\jmath}\hat{\jmath}}^{H}}{\partial \mathcal{X}}\right\} \tag{18}$$

As we can see, the core of the derivative of the objective function with respect to the DDF is located at the computation of the derivative of the homogenized elastic tensor $D^{H}_{\hat{i}\hat{i}\hat{j}\hat{j}}$. The derivations for the derivative of the homogenized stiffness tensor in detail can refer to [22,25,29], and the final form is given by:

$$\frac{\partial D^{H}_{\hat{i}\hat{i}\hat{j}\hat{j}}}{\partial \mathcal{X}} = \frac{1}{|\Omega|}\int_{\Omega}\left(\varepsilon^{0(\hat{i}\hat{i})}_{pq} - \varepsilon_{pq}\left(u^{\hat{i}\hat{i}}\right)\right)\gamma\left(\mathcal{X}(\boldsymbol{\rho})\right)^{\gamma-1} D^{0}_{pqrs}\left(\varepsilon^{0(\hat{j}\hat{j})}_{rs} - \varepsilon_{rs}\left(u^{\hat{j}\hat{j}}\right)\right) d\Omega \tag{19}$$

As pointed out in Section 4.1, the DDF is constructed by a linear combination of the NURBS basis functions with the smoothed nodal densities, and the smoothed nodal densities are obtained by the Shepard function to process nodal densities. The first-order derivatives of the DDF with respect to the nodal densities can be derived by:

$$\frac{\partial \mathcal{X}(\xi,\eta)}{\partial \rho_{i,j}} = \frac{\partial \mathcal{X}(\xi,\eta)}{\partial \mathcal{G}(\rho_{i,j})}\frac{\partial \mathcal{G}(\rho_{i,j})}{\partial \rho_{i,j}} = R^{p,q}_{i,j}(\xi,\eta)\psi(\rho_{i,j}) \tag{20}$$

where $R^{p,q}_{i,j}(\xi,\eta)$ is the NURBS basis function at the computational point (ξ,η). $\psi(\rho_{i,j})$ is the value of the Shepard function at the control point (i,j). It is important to note that the above computational point (ξ,η) is different from the control point (i,j). In Eq. (16), the computational points are Gauss quadrature points. According to the chain rule, the final form of the derivative of the homogenized elastic tensor with respect to the initial nodal densities can be computed by:

$$\frac{\partial D^{H}_{\hat{i}\hat{i}\hat{j}\hat{j}}}{\partial \mathcal{X}} = \frac{1}{|\Omega|}\int_{\Omega}\left(\varepsilon^{0(\hat{i}\hat{i})}_{pq} - \varepsilon_{pq}\left(u^{\hat{i}\hat{i}}\right)\right)\gamma\left(\mathcal{X}(\boldsymbol{\rho})\right)^{\gamma-1} D^{0}_{pqrs}\left(\varepsilon^{0(\hat{j}\hat{j})}_{rs} - \varepsilon_{rs}\left(u^{\hat{j}\hat{j}}\right)\right) R^{p,q}_{i,j}(\xi,\eta)\psi(\rho_{i,j})\, d\Omega \tag{21}$$

Hence, the first-order derivative of the objective function J with respect to design variables can be derived based on Eq. (21). Similarly, the derivatives of the volume constraint can be expressed by:

$$\frac{\partial G}{\partial \rho_{i,j}} = \frac{1}{|\Omega|}\int_{\Omega} R^{p,q}_{i,j}(\xi,\eta)\psi(\rho_{i,j})v_0\, d\Omega \tag{22}$$

According to Eqs. (18), (21) and (22), the first-order derivatives of the objective and constraint functions are strongly dependent on the NURBS basis functions at Gauss quadrature points and Shepard function at control points. In the optimization, the NURBS basis functions and Shepard function keep unchanged, and they can be pre-stored. Hence, the sensitivity analysis can reduce the computational cost in the optimization. Meanwhile, it is noticed that the above derivations are developed for 2D materials, which can be directly extended to 3D scenario.

5 A relaxed OC method

It is known that the OC method [64] has been widely employed in structural optimization problems [13] where a large number of design variables but only with a single resource constraint. Moreover, the objective and constraint functions need to satisfy certain monotonicity properties. However, the positive and negative sensitivities of the objective function with respect to the design variables can appear in the optimization of auxetic metamaterials considering the above formulation. In previous works [72], the damping factor has been eliminated, leading to a result that the volume fraction is inactive in the optimization process. Here, a relaxed OC method [65] is applied to update the design variables, and the corresponding update scheme is expressed as:

$$\rho_{i,j}^{(\vartheta+1)} = \begin{cases} max\left\{\left(\rho_{i,j}^{(\vartheta)} - m\right), \rho_{min}\right\}, & if \left(\left(\Pi_{i,j}^{(\vartheta)}\right)^{\varsigma} \rho_{i,j}^{(\vartheta)} \le max\left\{\left(\rho_{i,j}^{(\vartheta)} - m\right), \rho_{min}\right\}\right) \\ \left(\Pi_{i,j}^{(\vartheta)}\right)^{\varsigma} \rho_{i,j}^{(\vartheta)}, & if \left\{\begin{matrix} max\left\{\left(\rho_{i,j}^{(\vartheta)} - m\right), \rho_{min}\right\} < \left(\Pi_{i,j}^{(\vartheta)}\right)^{\varsigma} \rho_{i,j}^{(\vartheta)} \\ < min\left\{\left(\rho_{i,j}^{(\vartheta)} + m\right), 1\right\} \end{matrix}\right\} \\ min\left\{\left(\rho_{i,j}^{(\vartheta)} + m\right), 1\right\}, & if \left(min\left\{\left(\rho_{i,j}^{(\vartheta)} + m\right), 1\right\} \le \left(\Pi_{i,j}^{(\vartheta)}\right)^{\varsigma} \rho_{i,j}^{(\vartheta)}\right) \end{cases} \tag{23}$$

where m and ς are the move limit and the damping factor, respectively. The Lagrange multiplier $\Lambda^{(\vartheta)}$ at the ϑ^{th} iteration step can be updated by a bi-sectioning algorithm [13]. The updating factor $\Pi_{i,j}^{(\vartheta)}$ for the $(i,j)_{th}$ design variable at the ϑ^{th} iteration step can be defined as:

$$\Pi_{i,j}^{(\vartheta)} = \frac{1}{\Lambda^{(\vartheta)} + \mu^{(\vartheta)}}\left(\mu^{(\vartheta)} - \frac{\partial J}{\partial \rho_{i,j}^{(\vartheta)}} \Big/ max\left(\Delta, \frac{\partial G}{\partial \rho_{i,j}^{(\vartheta)}}\right)\right) \tag{24}$$

where Δ is a small positive constant to avoid the fraction with a form of $0/0$. The updating factor $\Pi_{i,j}^{(\vartheta)}$ can be positive in the optimization, by choosing an appropriate value of the shift parameter $\mu^{(\vartheta)}$, namely:

$$\mu^{(\vartheta)} \ge max\left\{\frac{\partial J}{\partial \rho_{i,j}^{(\vartheta)}} \Big/ max\left(\Delta, \frac{\partial G}{\partial \rho_{i,j}^{(\vartheta)}}\right)\right\} \ (i = 1,2,\cdots,n; j = 1,2,\cdots,m) \tag{25}$$

A systematic flowchart of the ITO formulation for auxetic metamaterials is shown in **Fig. 5**, and the detailed steps are listed as follows:

Step 01: Input initial parameters: structural sizes, NURBS basis functions; knot vector and so on;

Step 02: Construct geometrical model (CAD) of the structure by NURBS;

Step 03: Construct numerical analysis model (CAE) of the structure, namely IGA mesh;

Step 04: Construct the initial DDF by NURBS basis functions and Shepard function;

Step 05: Impose PBCs on the microstructure and apply IGA to solve the displacement field;

Step 06: IGA-based EBHM to evaluate the homogenized elastic tensor;

Step 07: Calculate the objective function and volume fraction;

Step 08: Calculate the derivatives of the objective and constraint functions;

Step 09: Update the design variables and DDF by the relaxed OC method;

Step 10: Check convergence; if not, go back to **Step 05**; if yes, go to **Step 11**;

Step 11: End and Output auxetic metamaterials.

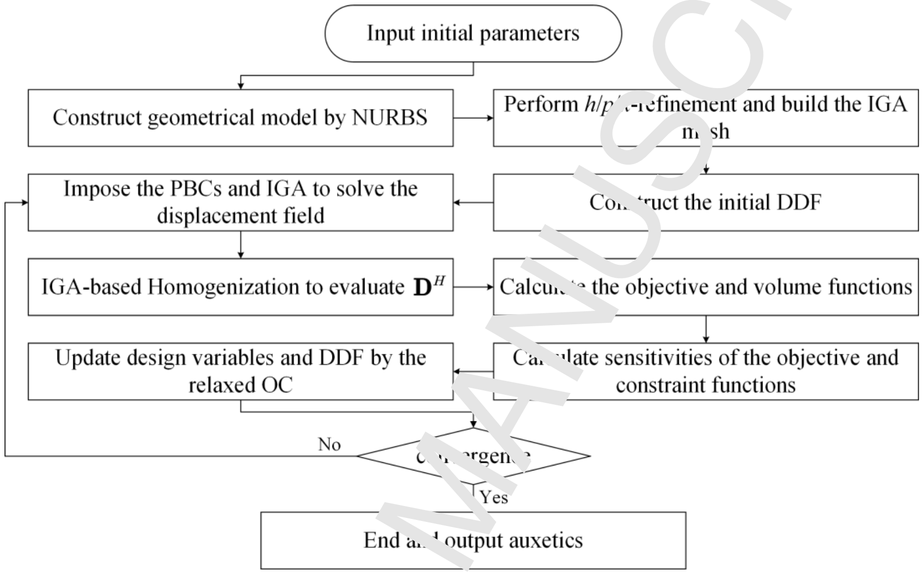

Fig. 5. The flowchart of the ITO formulation for auxetic metamaterials

6. Numerical Examples

In this section, several numerical examples are provided to demonstrate the effectiveness and efficiency of the ITO method for auxetic metamaterials. 2D auxetic microstructures are firstly studied to show the basic features of the developed ITO method. Secondly, the ITO method is applied to discuss the optimization of 3D material microstructures with the auxetic behavior to demonstrate its superior effectiveness. Finally, the auxetic behavior of the topologically-optimized 3D material microstructures are validated in the software ANSYS and the 3D auxetic metamaterials are also prototyped by using the 3D printing technique. Only the linearly elastic materials are considered, and 2D microstructures will be discretized by the plane stress elements. In all examples, the Young's moduli E_0 and the Poisson's ratio υ_0 for the basis material are defined as 1 and 0.3, respectively. In the numerical analysis, 3×3 (2D) or 3×3×3 (3D) Gauss quadrature points are chosen in an IGA element. For numerical simplicity, the dimensions of material microstructures in all directions are set to be 1. The penalty parameter in Section 4.2 is set as 3. The constant parameter β in all numerical examples is set to be 0.03, expect the specific definition. The terminal criterion is that the

L_∞ norm of the difference of the nodal densities between two consecutive iterations is less than 1% or the maximum 100 iteration steps are reached.

6.1 2D auxetic metamaterials

Considering 2D materials, the structural design domain is a square with 1×1, shown in **Fig. 1** (*a*). Here, NURBS surface is applied to parametrize the design domain, where the quadratic NURBS basis functions are chosen and the knot vectors are set as: $\Xi = \mathcal{H} = \{0,0,0,0.01,\cdots,0.99,1,1,1\}$. The corresponding IGA mesh for the design domain has 100×100 elements, and 101×101 (10202) control points are contained in the NURBS surface. The maximum material consumption V_0 is defined as 30%. As already described in Section 4, the developed ITO method aims to optimize the densities in the DDF to represent the evolving of the structural topology, until auxetic microstructures can be achieved. As given in Eq. (14), the DDF is constructed by the NURBS, which can be viewed as a density response surface in spatial for nodal densities. The initial design of material microstructure is displayed in **Fig. 6**, including the nodal densities at control points in **Fig. 6** (*a*), the densities at Gauss quadrature points in **Fig. 6** (*b*) and the density response surface of the DDF in **Fig. 6** (*c*). It should be noted that the height direction denotes the density value in **Fig. 6**. It can be easily found that the initial design of material microstructure is homogenously occupied with some holes to avoid the uniformly distributed sensitivity field, owing to the imposing of the periodic boundary conditions on material microstructure.

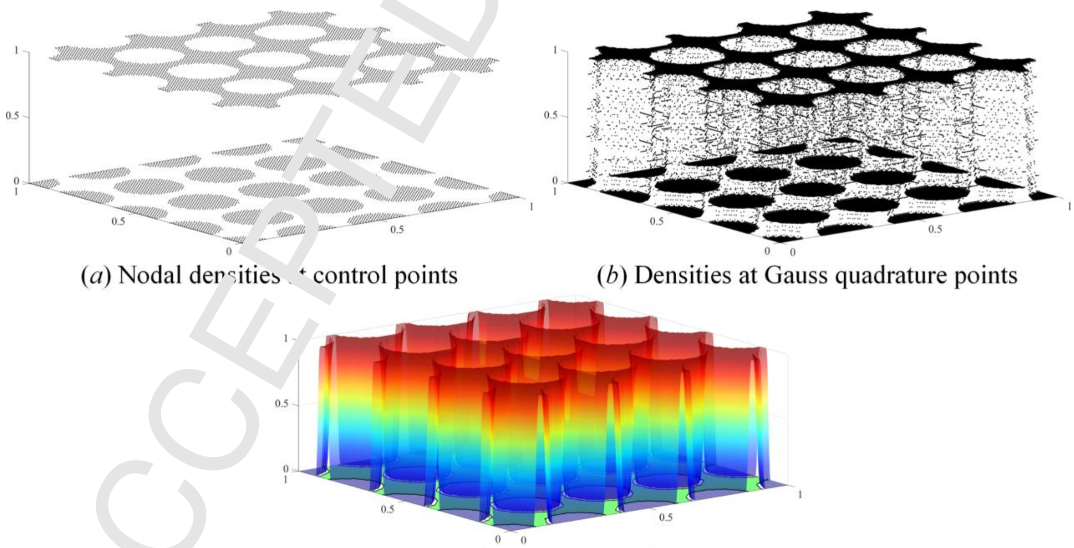

(*a*) Nodal densities at control points (*b*) Densities at Gauss quadrature points

(*c*) Density response surface

Fig. 6. The initial design of material microstructure

As shown in **Fig. 7**, the optimized designs of material microstructure are provided, including the optimized densities at Gauss quadrature points in **Fig. 7** (*a*) and the optimized density response surface of the DDF in

Fig. 7 (*b*). It can be easily found that the optimized densities at Gauss quadrature points and the optimized density response are both featured with the sufficient smoothness and continuity. The main cause is that the Shepard function and NURBS basis functions are considered in the construction of the DDF. The former can guarantee the smoothness of the DDF by improving the overall smoothness of nodal densities, and the latter ensure its continuity. In order to show the details of the optimization of the DDF, we provide a series of intermediate density response surfaces of the DDF during the process. As shown in **Fig. 6** (*c*) and **Fig. 8** (*a*), the initial density response surface has a break from 0 to 1. During the optimization, the smoothness is gradually improved with the consideration of the Shepard function in the construction of the DDF, explicitly represented by the transition part of the surface from 0 to 1. Additionally, the optimized densities of the DDF in material microstructure are distributed nearly 0 and 1, owing to the penalty parameter, and the key principle of the penalty mechanism in topology optimization can refer to [16].

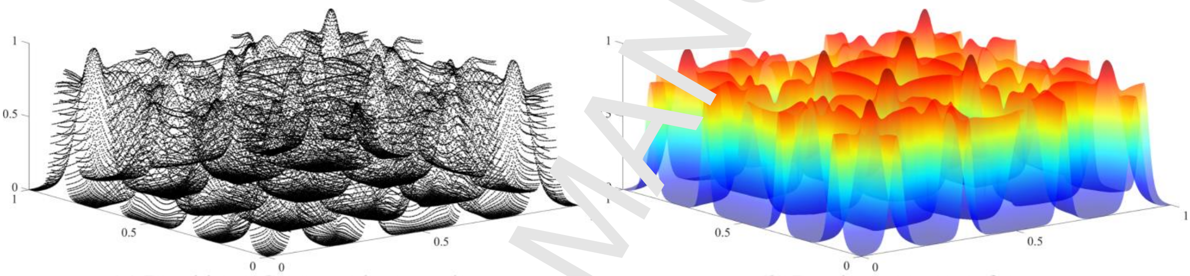

(*a*) Densities at Gauss quadrature points (*b*) Density response surface

Fig. 7. The optimized designs of material microstructure

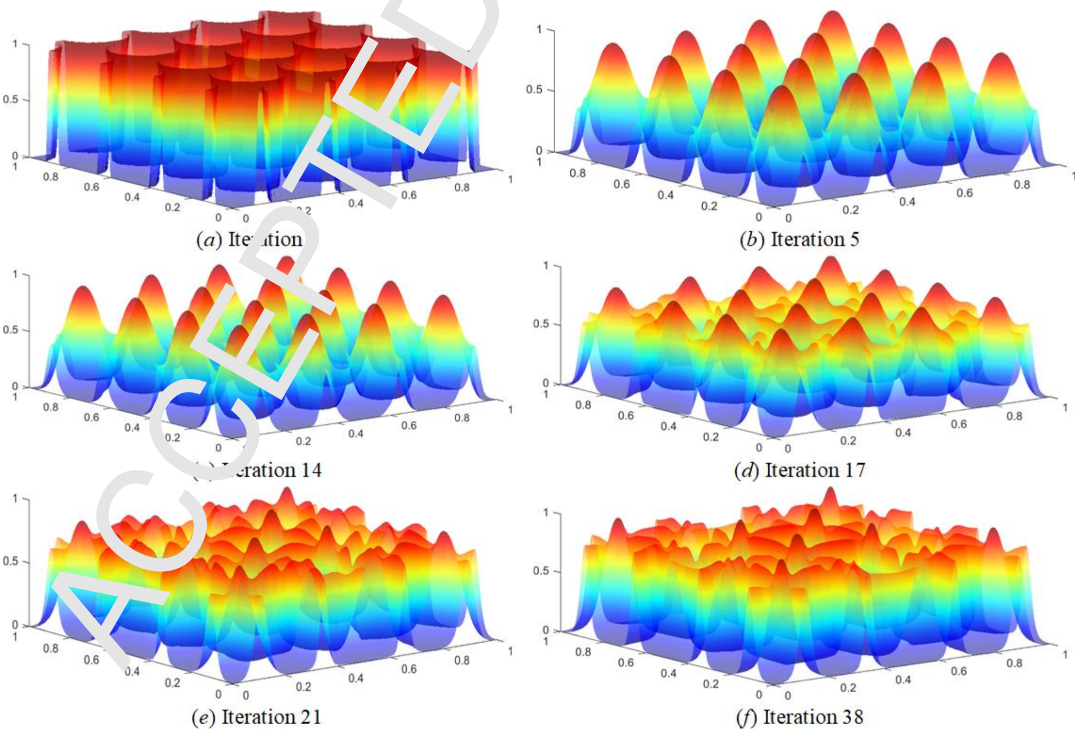

(*a*) Iteration (*b*) Iteration 5 (*c*) Iteration 14 (*d*) Iteration 17 (*e*) Iteration 21 (*f*) Iteration 38

Fig. 8. Intermediate density response surfaces of the DDF

As shown in **Fig. 8**, the evolving of the DDF represent the topological changes during the optimization. In order to obtain an appropriate configuration of material microstructure using the DDF, a heuristic scheme is introduced to define the structure topology. The mathematical model is defined in Eq. (26), where $\mathcal{X}_c$ is a constant, expressed as:

$$\begin{cases} 0 \leq \mathcal{X}(\xi,\eta) < \mathcal{X}_c & void \\ \mathcal{X}(\xi,\eta) = \mathcal{X}_c & boundary \\ \mathcal{X}_c < \mathcal{X}(\xi,\eta) \leq 1 & solid \end{cases} \tag{26}$$

As we can see, the structural boundaries of material microstructure are expressed by the iso-contour of the DDF. The DDF with the densities higher than $\mathcal{X}_c$ describes solids in the structural design domain, and the densities lower than $\mathcal{X}_c$ is used to present voids. We can easily find that the current scheme to define the structural topology using the DDF is analogous to the implicit boundary representation model in the LSM [18–20]. However, it is important to notice that the proposed ITO method for auxetic metamaterials is not developed in a framework of the Hamilton-Jacobi partial differential equation to track the advancing of the structural boundary. Eq. (26) can be just viewed as a post-processing mechanism to define the topology using the DDF, and the core of the developed ITO method for auxetic metamaterials is the optimization of the DDF to represent the topological changes.

In the work, the constant $\mathcal{X}_c$ is set to be 0.5. According to **Fig. 7**, we can see that the 0.5 is a relatively suitable value to define the topology, due to a phenomenon that most densities are distributed nearly 0 or 1 ($[0, 0.2]$ and $[0.8, 1]$). The corresponding numerical results of material microstructure are listed in **Table 1**, including the 2D view of densities at Gauss quadrature points but with only higher than 0.5, the optimized topology, the homogenized elastic tensor $\mathbf{D}^H$, the corresponding negative Poisson's ratio $\upsilon = -0.61$ and the volume fraction of the optimized topology $V_f = 29.88\%$. The volume fraction of the final topology is mostly close to the prescribed volume fraction 30%, which shows the appropriateness of the threshold value 0.5 to define the topology using the DDF. The topologically-optimized design of material microstructure with the negative Poisson ratio -0.61 also shows the effectiveness of the current ITO method on seeking for 2D auxetic metamaterials. As given in **Fig. 9**, two rotating mechanisms related to the generation of the auxetic behavior in material microstructures are given, which demonstrates the rationality of the definition of the objective function with the consideration of the term $\sum_{\hat{\imath},\hat{\jmath}=1,\hat{\imath}=\hat{\jmath}}^{d} D^H_{\hat{\imath}\hat{\imath}\hat{\jmath}\hat{\jmath}}$.

Additionally, it can be easily found that the optimized topology is featured with the smooth boundaries and clear interfaces between solids and voids owing to the DDF with the sufficient smoothness and continuity, which can be beneficial to lower the difficulties for the latter manufacturing. Although the ITO method for auxetic metamaterials is developed on the basis of the conception of material densities, the key intention of the ITO formulation is to seek for the optimal DDF with the auxetic characteristic. Finally, the convergent curves of the objective function and volume fraction of the DDF are shown in **Fig. 10** with the intermediate topologies of 2D auxetic microstructure. It can be easily found that the iterative histories are very smooth, and the optimization can quickly arrive at the prescribed convergent condition within 38 steps, which shows the perfect stability of the proposed ITO method on the optimization of 2D auxetics.

Table 1. The optimized 2D auxetic metamaterial

2D view of densities	Topology	$\mathbf{D}^H$	υ	V_f
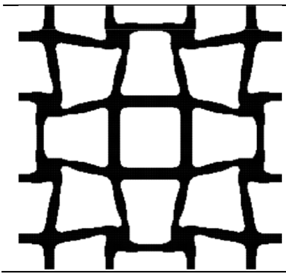	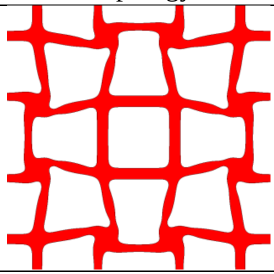	$\begin{bmatrix} 0.088 & -0.054 & 0 \\ -0.054 & 0.088 & 0 \\ 0 & 0 & 0.0027 \end{bmatrix}$	-0.61	29.88%

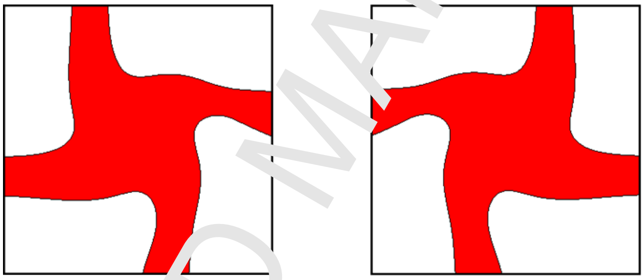

Fig. 9. Rotating mechanisms in the optimized 2D auxetic metamaterial

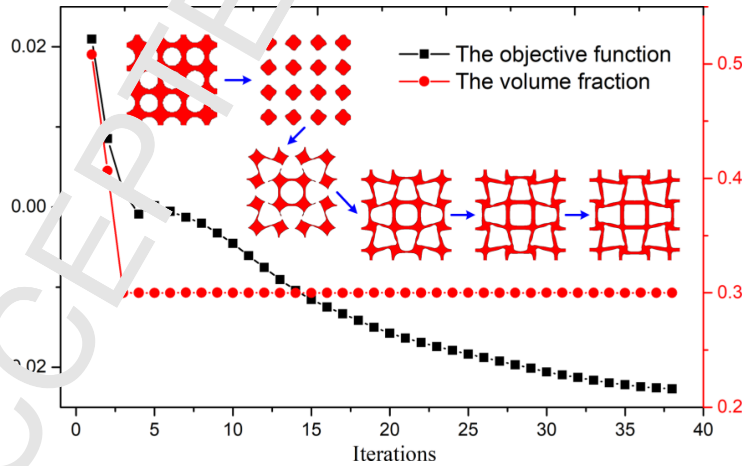

Fig. 10. Iterative curves of 2D auxetic metamaterial

6.2 Discussions of the weight parameter

In this section, we study the effect of the weight parameter β in the objective function on the optimization of auxetic metamaterials. The weight parameter β will be discussed with 15 cases, namely 0.03 (Section

6.1), 0.04, 0.05, 0.06, 0.07, 0.08, 0.09, 0.10, 0.15, 0.20, 0.25, 0.30, 0.0001, 0.0005, 0.02. The related design parameters are consistent with Section 6.1, like the NURBS details, the maximum material consumption, the initial design and etc.

As shown in **Fig. 11**, the corresponding numerical results of the former twelve cases from 0.03 to 0.30 are firstly provided. It can be found that the values of the Poisson's ratio in twelve cases are increased with the increasing of the weight parameter. The corresponding auxetic microstructures in the twelve cases are shown in **Fig. 12**. The auxetic behavior is becoming smaller and smaller with the increasing of the weight parameter. When the weight parameter is equal to 0.3, the optimized material microstructure is not featured with the negative Poisson's ratio. Meanwhile, the first case with the weight parameter 0.03 can obtain auxetic microstructure with the minimum negative Poisson's ratio -0.614 in the similar iterative steps when compared to other cases.

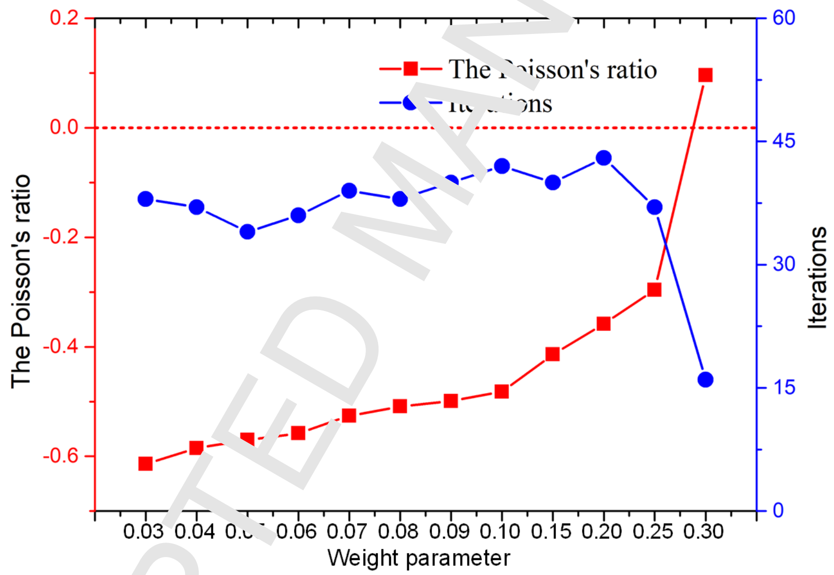

Fig. 11. Numerical results of the former twelve cases

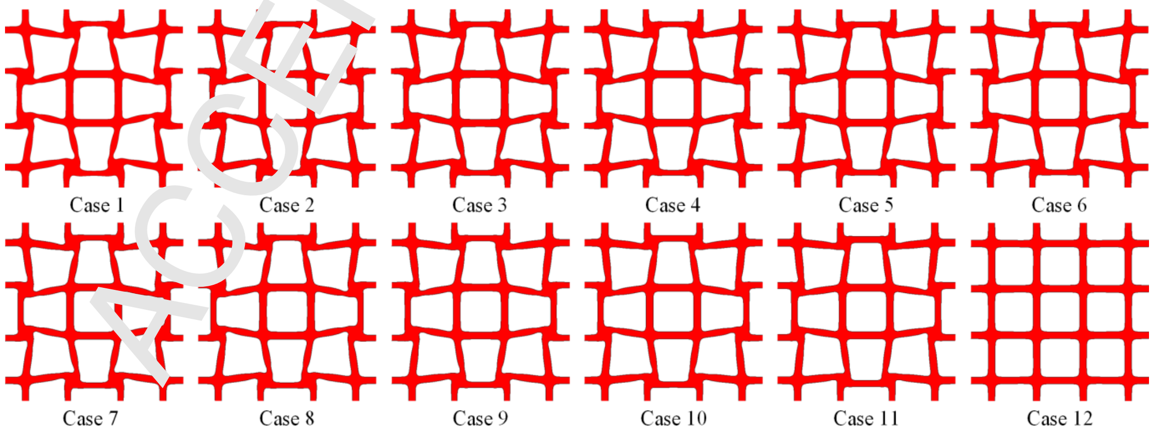

Fig. 12. Auxetic microstructures in twelve cases

Three numerical cases with the weight parameter equal to 0.02, 0.005 and 0.0001, respectively, are provided in **Table 2**. If the weight parameter is decreased, the optimizer intends to minimize the negative Poisson's ratio in one direction. As listed in the third row of **Table 2**, namely $\beta = 0.0005$, the υ_{21} is smaller than the υ_{12}, and the auxetic microstructure is the orthotropic. However, if the weight parameter is very small, equal to 0.0001, the final auxetic metamaterial is the anisotropic. The auxetic behavior of the design results from the chiral deformation mechanism. The above phenomenon mainly stems from a fact that the weight parameter controls the influence degree of the term $\sum_{\hat{\imath},\hat{\jmath}=1,\hat{\imath}=\hat{\jmath}}^{d} D_{\hat{\imath}\hat{\imath}\hat{\jmath}\hat{\jmath}}^{H}$ in the objective function. Additionally, as shown in the last column of **Table 2**, we can confirm that an increasing number of iterations are required to arrive at the convergent criterion in the optimization, with the decreasing of the weight parameter. Hence, as far as finding auxetic microstructures with the identical negative Poisson's ratios in two directions, the weight parameter 0.03 is a relatively appropriate value for the ITO method. It should be noted that the discussion for the weight parameter is just suitable for the current ITO method.

Table 2. Numerical results of three cases.

β	Topology	Homogenized elastic tensor $\mathbf{D}^H$	υ	Iterations
0.02	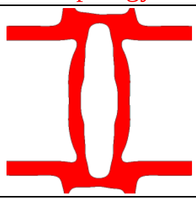	$\begin{bmatrix} 0.0762 & -0.038 & 0 \\ -0.038 & 0.0702 & 0 \\ 0 & 0 & 0.0008 \end{bmatrix}$	$\begin{cases} \upsilon_{12} = -0.498 \\ \upsilon_{21} = -0.541 \end{cases}$	117
0.0005	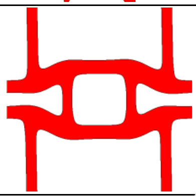	$\begin{bmatrix} 0.1204 & -0.053 & 0 \\ -0.053 & 0.0392 & 0 \\ 0 & 0 & 0.0011 \end{bmatrix}$	$\begin{cases} \upsilon_{12} = -0.442 \\ \upsilon_{21} = -1.352 \end{cases}$	101
0.0001	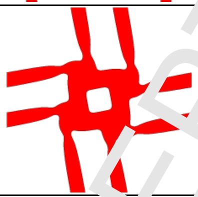	$\begin{bmatrix} 0.084 & -0.057 & 0.013 \\ -0.057 & 0.085 & -0.013 \\ 0.013 & -0.013 & 0.0028 \end{bmatrix}$	$\begin{cases} \upsilon_{12} = -0.678 \\ \upsilon_{21} = -0.671 \end{cases}$	157

6.3 3D auxetic metamaterials

In this section, the optimization of 3D auxetic metamaterials is studied to present the superior effectiveness of the developed ITO method. As far as 3D material microstructure, the design domain is a cubic with $1\times1\times1$, as shown in **Fig. 13** (*a*). The structural design domain is parameterized by the NURBS solid, where the quadratic NURBS basis functions are used and the knot vectors in three parametric directions are set as $\Xi = \mathcal{H} = \mathcal{Z} = \{0,0,0,0.417,\cdots,0.9583,1,1,1\}$. The NURBS solid and the IGA mesh for the design domain are displayed in **Fig. 13** (*b*) and (*c*), respectively. The IGA mesh has 24×24×24 elements, and 26×26×26 control points are included in the NURBS solid. The total number of design variables is equal to 26×26×26. An IGA element contains 3×3×3 Gauss quadrature points, and the total number of Gauss quadrature points is equal to 72×72×72. In this section, four different initial designs of 3D material microstructure are defined and four causes will be studied. For 3D material microstructure, it is difficult to plot the 4D density response surface. We only display the correponding iso-contours of four initial material microstructures, as given in **Fig. 14**, where $\mathcal{X}_c$ is still set to be 0.5.

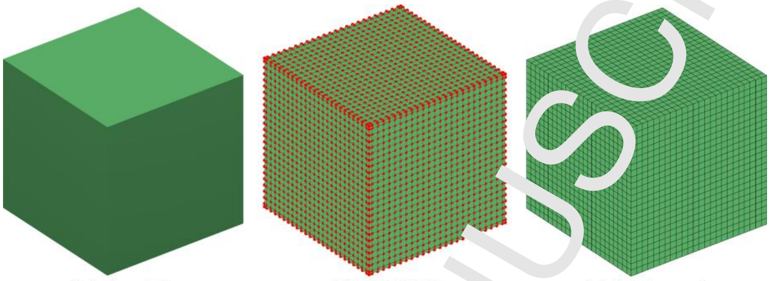
(*a*) A cubic (*b*) NURBS (*c*) IGA mesh

Fig. 13. 3D material microstructure

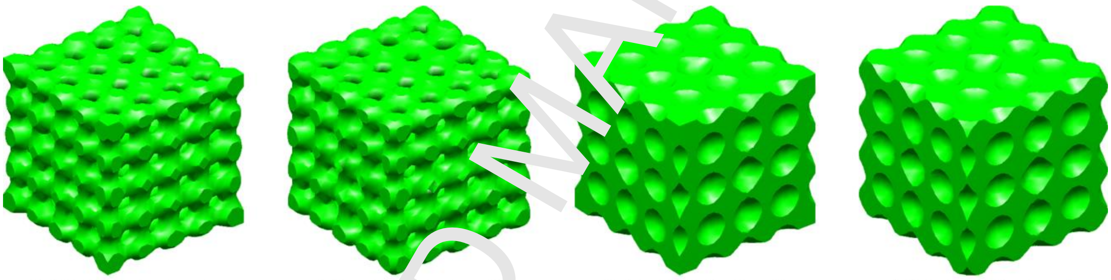
(*a*) initial design 1 (*b*) initial design 2 (*c*) initial design 3 (*d*) initial design 4

Fig. 14. Four initial designs for 3D material microstructure

The initial design 1 shown in **Fig. 14** (*a*) is considered in Case 1, where the maximum material consumption is set to be 30%. As clearly displayed in **Fig. 15** (*a*), the optimized topology of 3D material microstructure with the auxetic behavior is provided. In order to observe the interior configuration of the optimized design, the middle cross-sectional view of the 3D auxetic microstructure is presented in **Fig. 15** (*b*). Meanwhile, a 3D auxetic metamaterial with 3×3×3 repetitive microstructures is shown in **Fig. 15** (*c*). It can be easily seen that the optimized 3D auxetic microstructure is characterized with the smooth boundaries and distinct interfaces between the solids and voids, originating from the constructed DDF with the desired smoothness and continuity. Meanwhile, it can be easily observed that the 3D material microstructure shown in **Fig. 15** (*a*) can exhibit the counterintuitive dilatational behavior, when a load is imposed on one direction of this structure. As listed in **Table 3**, the homogenized elastic tensor of the 3D material microstructure in **Fig. 15** (*a*) is given and the corresponding Poisson's ratio is equal to -0.047. Hence, the auxetic behavior of the 3D microstructure 1 can be confirmed from not only the qualitative analysis, but also quantitative calculation.

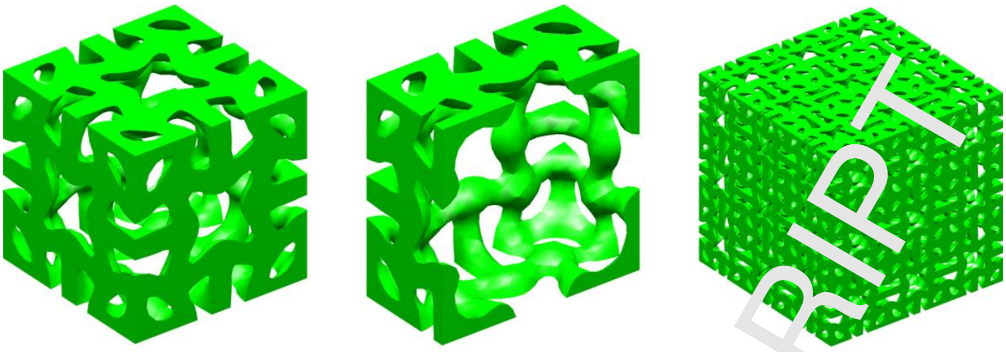

(*a*) Topology (*b*) Half topology (*c*) 3×3×3 topologies

Fig. 15. 3D auxetic microstructure No. 1

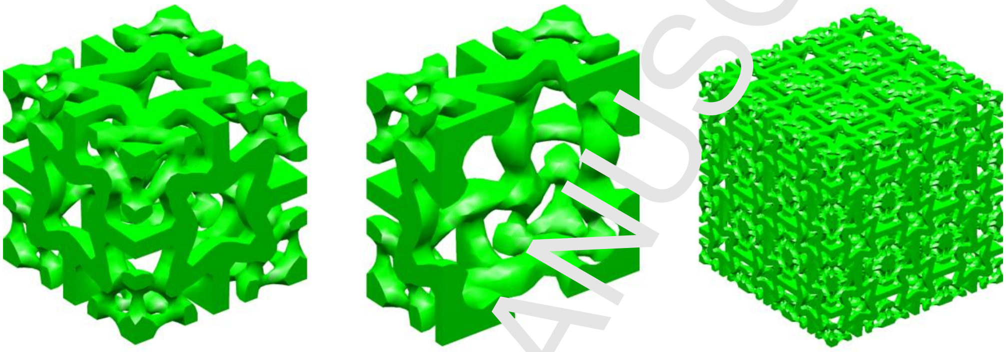

(*a*) Topology (*b*) Half topology (*c*) 3×3×3 topologies

Fig. 16. 3D auxetic microstructure No. 2

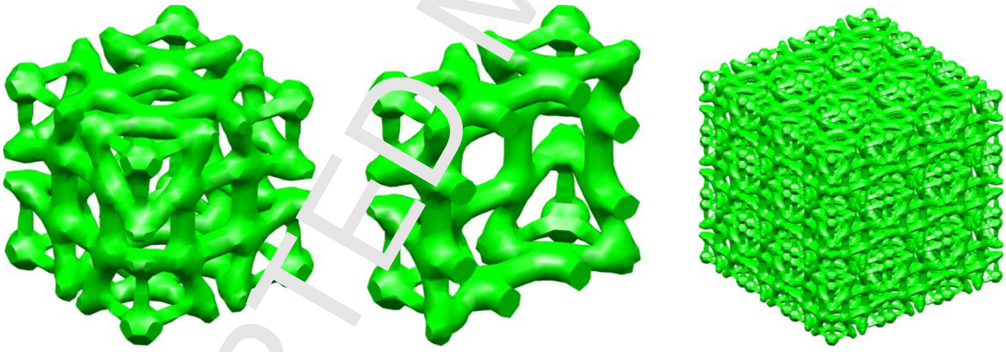

(*a*) Topology (*b*) Half topology (*c*) 3×3×3 topologies

Fig. 17. 3D auxetic microstructure No. 3

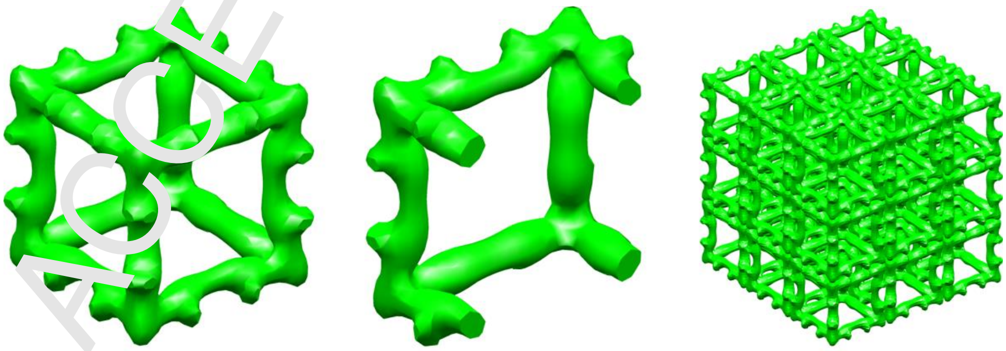

(*a*) Topology (*b*) Half topology (*c*) 3×3×3 topologies

Fig. 18. 3D auxetic microstructure No. 4

Similarly, Case 2 is performed with the maximum volume fraction 30%, starting from the initial design 2, shown in **Fig. 14** (*b*). The initial design 3, illustrated in **Fig. 14** (*c*), is considered in Case 3 also with the maximum material consumption 30%, and Case 4 optimizes the 3D microstructure starting from the initial design 4 displayed in **Fig. 14** (*d*), but with the maximum volume fraction 24%. The final optimized results in Cases 2, 3 and 4 are displayed in **Fig. 16**, **17** and **18**, respectively, also including the optimized topology, the cross-sectional view of the topology to illustrate the interior information in detail and 3×3×3 repetitive distributed auxetic microstructures. The homogenized elastic tensors of 3D auxetic microstructures 2, 3 and 4 are listed in **Table 3**, where the corresponding Poisson's ratio are also computed, namely -0.082, -0.12, -0.11. Thereby, the capability of the ITO method to seek for 3D auxetic metamaterials can be presented.

Table 3. The homogenized elastic tensors of four 3D auxetic microstructures

3D auxetic microstructure 1	3D auxetic microstructure 2
$\begin{bmatrix} 0.045 & -0.0021 & -0.0021 & 0 & 0 & 0 \\ -0.0021 & 0.045 & -0.0122 & 0 & 0 & 0 \\ -0.0021 & -0.0021 & 0.045 & 0 & 0 & 0 \\ 0 & 0 & 0 & 0.0031 & 0 & 0 \\ 0 & 0 & 0 & 0 & 0.0031 & 0 \\ 0 & 0 & 0 & 0 & 0 & 0.0031 \end{bmatrix}$ $\upsilon = -0.047$	$\begin{bmatrix} 0.0788 & -0.0065 & -0.0065 & 0 & 0 & 0 \\ -0.0065 & 0.0788 & -0.0065 & 0 & 0 & 0 \\ -0.0065 & -0.0065 & 0.0788 & 0 & 0 & 0 \\ 0 & 0 & 0 & 0.0052 & 0 & 0 \\ 0 & 0 & 0 & 0 & 0.0052 & 0 \\ 0 & 0 & 0 & 0 & 0 & 0.0052 \end{bmatrix}$ $\upsilon = -0.082$
3D auxetic microstructure 3	**3D auxetic microstructure 4**
$\begin{bmatrix} 0.0789 & -0.0094 & -0.0094 & 0 & 0 & 0 \\ -0.0094 & 0.0789 & -0.0094 & 0 & 0 & 0 \\ -0.0094 & -0.0094 & 0.0789 & 0 & 0 & 0 \\ 0 & 0 & 0 & 0.006 & 0 & 0 \\ 0 & 0 & 0 & 0 & 0.006 & 0 \\ 0 & 0 & 0 & 0 & 0 & 0.006 \end{bmatrix}$ $\upsilon = -0.12$	$\begin{bmatrix} 0.0331 & -0.0038 & -0.0038 & 0 & 0 & 0 \\ -0.0038 & 0.0331 & -0.0038 & 0 & 0 & 0 \\ -0.0038 & -0.0038 & 0.0331 & 0 & 0 & 0 \\ 0 & 0 & 0 & 0.0024 & 0 & 0 \\ 0 & 0 & 0 & 0 & 0.0024 & 0 \\ 0 & 0 & 0 & 0 & 0 & 0.0024 \end{bmatrix}$ $\upsilon = -0.11$

As shown **Fig. 19**, the 2D views of the topologically-optimized 3D auxetic microstructures are provided, which are analogous to the reported 2D auxetic microstructures in previous works [29,32]. However, it is not straight to extend the optimization for 2D auxetic metamaterials to 3D scenario. The convergent curves of the objective function, the volume fraction of the DDF and the topological change between two adjacent iterations in Cases 1 and 2 are displayed in **Fig. 20**. It can be easily found that the iterative histories in two cases are very smooth and quickly arrive at the prescribed convergent criterion, only 34 steps in Case 1 and 51 steps in Case 2. The intermediate topologies of the 3D auxetic microstructures in Case 1 and 2 are also displayed in **Fig. 21** and **22**, respectively. Hence, the effectiveness and efficiency of the ITO method on the optimization of 3D auxetic metamaterials can be demonstrated. Meanwhile, the pre-defined geometrical symmetries are not considered in the optimization to allow more freedoms to seek for the novel 3D auxetic microstructures. As shown in **Fig. 15**-**18**, a series of interesting 3D auxetic microstructures can be achieved in the current work. However, the negative Poisson's ratios of the optimized 3D auxetic microstructures are larger than the reported designs [28,34,35]. The negative Poisson's ratio of the auxetic microstructure strongly depends on the objective function. In Eq. (16), the objective function is expressed by a combination of the homogenized elastic tensor, which can only provide a reasonable search direction for the optimizer to find auxetic metamaterials. It is difficult to arrive at the expected negative Poisson's ratio. It should be noted that this phenomenon has a negligible influence on the latter applications of the ITO method, owing to the fact that the proposed ITO method can achieve topological design of auxetic metamaterials in a more effective and efficient manner. Based on the skeleton of the current topologically optimized designs (**Fig. 15-18)**, the auxetic metamaterials with any given negative Poisson's ratio can be achieved by further using shape optimization, similar to [34].

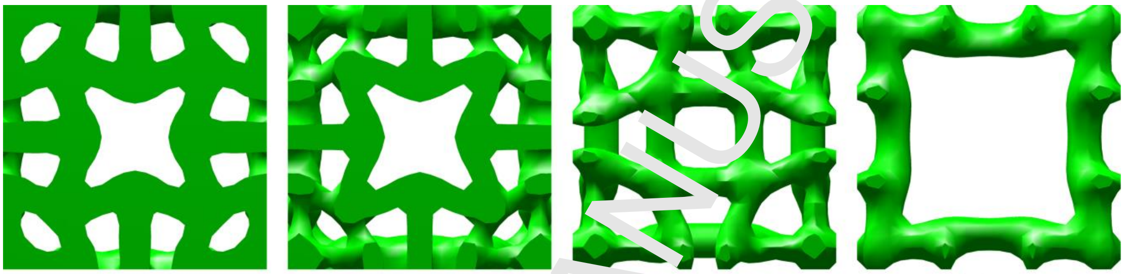

(*a*) Case 1 (*b*) Case 2 (*c*) Case 3 (*d*) Case 4

Fig. 19. The 2D-views for four auxetic microstructures

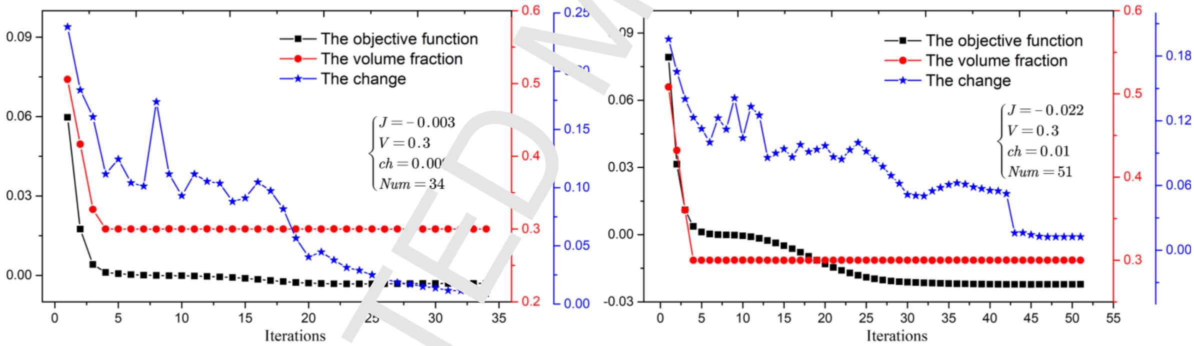

(*a*) Convergent curves of case 1 (*b*) Convergent curves of case 2

Fig. 20. Convergent histories of Cases 1 and 2

According to the discussion about the weight parameter in Section 6.2, two different cases with $\beta = 0.02$ and 0.0001 for 3D auxetic metamaterials are discussed, respectively. The optimized 3D auxetic designs in two cases are displayed in **Fig. 23**, including the optimized topologies and the cross-sectional views of the topologies. It can be easily seen that the 3D auxetic microstructure 5 in **Fig. 23** (*a*) is similar to the reported microstructure in [35]. The 3D auxetic microstructure No. 6 with the anisotropic is a new finding with the chiral deformation mechanism to form the auxetic behavior. The homogenized elastic tensors of two 3D auxetic microstructures are listed in **Table 4**, and the minimum Poisson's ratios of two cases are equal to -0.257 and -0.188, respectively.

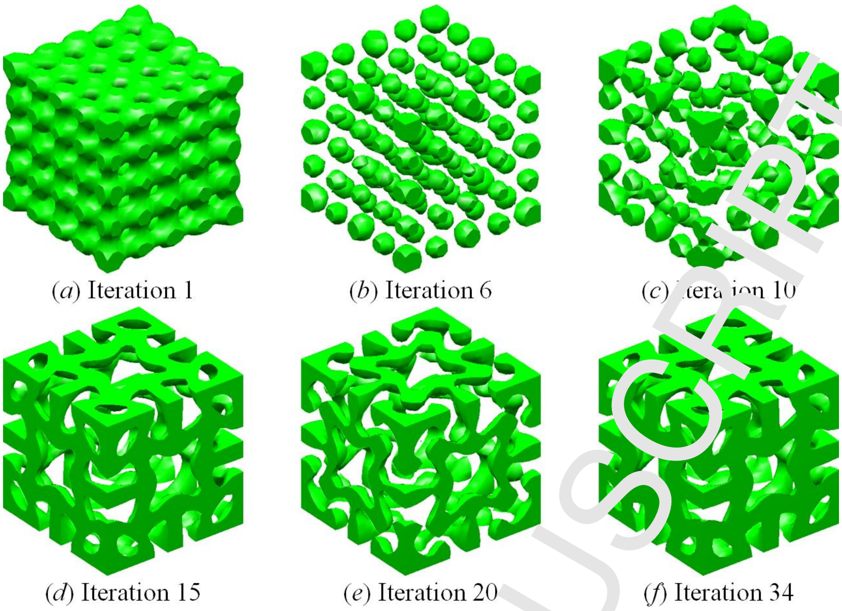

Fig. 21. Intermediate results of Case 1

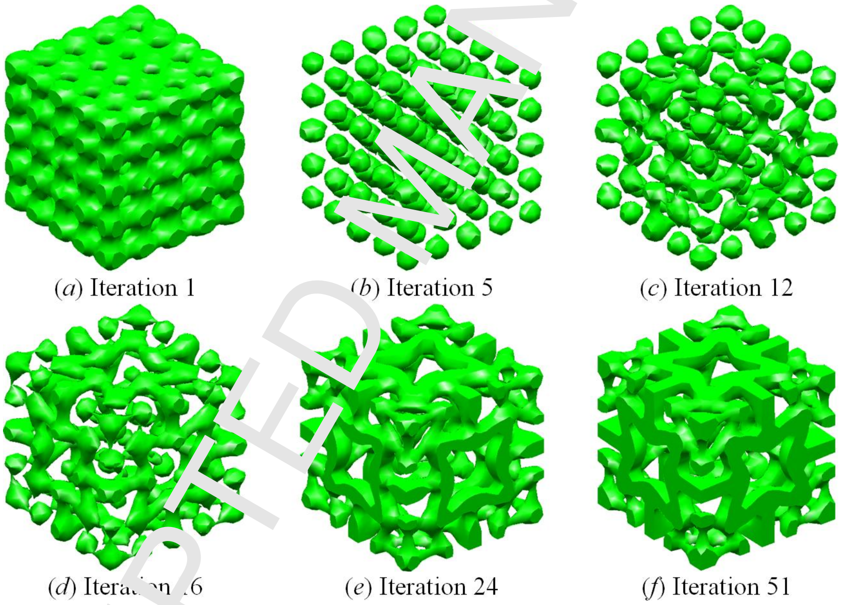

Fig. 22. Intermediate results of Case 2

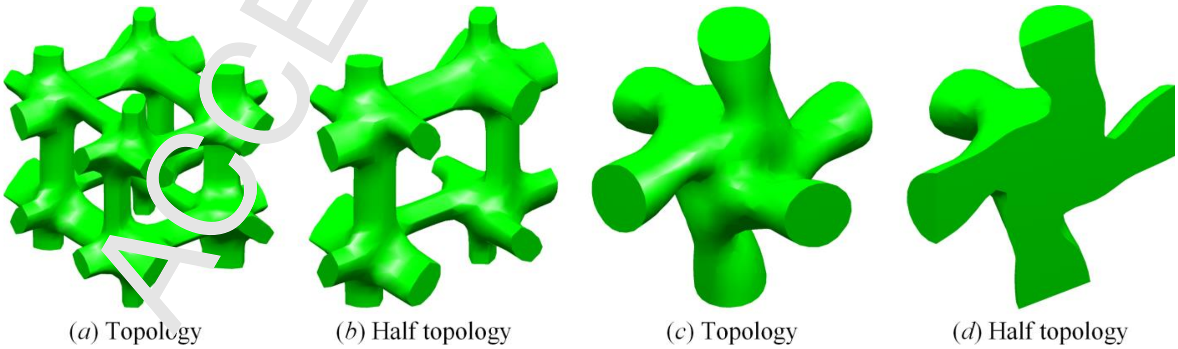

Fig. 23. 3D auxetic microstructures No. 5 and 6

Table 4. Homogenized elastic tensors of 3D auxetic microstructures No. 5 and 6.

3D auxetic microstructure 5	3D auxetic microstructure 6
$\begin{bmatrix} 0.0483 & -0.0124 & -0.0049 & 0 & 0 & 0 \\ -0.0124 & 0.0633 & -0.0122 & 0 & 0 & 0 \\ -0.0049 & -0.0122 & 0.0505 & 0 & 0 & 0 \\ 0 & 0 & 0 & 0.0047 & 0 & 0 \\ 0 & 0 & 0 & 0 & 0.0048 & 0 \\ 0 & 0 & 0 & 0 & 0 & 0.0047 \end{bmatrix}$	$\begin{bmatrix} 0.0457 & -0.0028 & -0.008 & 0.0031 & 0.0009 & 0.0067 \\ -0.0028 & 0.0426 & -0.0062 & -0.0032 & -0.0062 & -0.0004 \\ -0.008 & -0.0062 & 0.053 & -0.0003 & 0.0045 & -0.0053 \\ 0.0031 & -0.0032 & -0.0003 & 0.0004 & -0.0002 & -0.0002 \\ 0.0009 & -0.0062 & 0.0045 & -0.0002 & 0.0038 & 0.0004 \\ 0.0067 & -0.0004 & -0.0053 & -0.0002 & 0.0004 & 0.0038 \end{bmatrix}$
$\upsilon_{min} = -0.257$	$\upsilon_{min} = -0.$[illegible]88

6.4 Simulating validation based on ANSYS

In this section, the numerical verification of the above optimized auxetic microstructures is performed using ANSYS, and the auxetic microstructure No. 1 is considered. The “STL” file of the auxetic microstructure No. 1, as shown in **Fig. 24 (*a*)**, is firstly exported from Matlab and then imported into ANSYS. The “STL” file needs to be slightly modified in the SpaceClaim of ANSYS and converted into the solid geometry with 1cm×1cm×1cm, given in **Fig. 24 (*b*)**. The volume fraction of the “STL” file for 3D auxetic microstructure 1 is equal to 29.65% (nearly 30%) and the volume fraction 29.73% of the modified solid geometry is also mostly identical to 30%. In order to test the negative Poisson's ratio with a much higher accuracy, an auxetic metamaterial with 5×5×5 auxetic microstructures No. 1 is considered in the latter simulation, as shown in **Fig. 25 (*a*)**, and the corresponding mesh is also shown in **Fig. 25 (*b*)** with 19763500 finite elements.

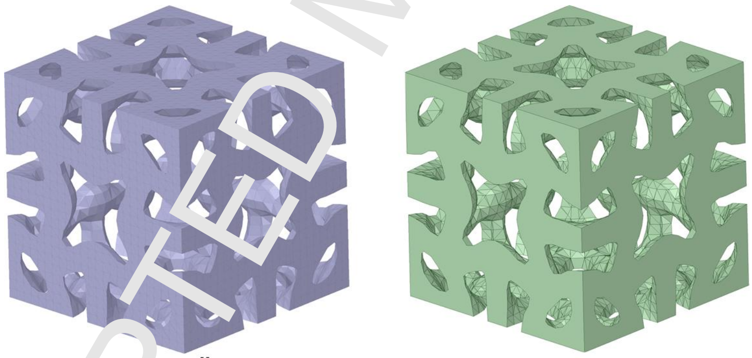

(*a*) “STL” file (*b*) Solid geometry

Fig. 24. 3D auxetic microstructure No. 1

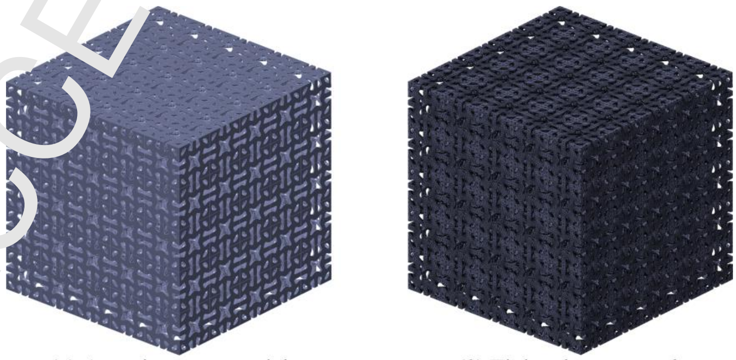

(*a*) Auxetic metamaterial (*b*) Finite element mesh

Fig. 25. Auxetic metamaterial and its finite element mesh

In **Fig. 26**, three boundary conditions are imposed on the auxetic metamaterial. Condition 1, shown in **Fig. 26** (*a*), fixes the Z-direction displacements of the surface A with the normal direction Z-. In the Condition 2, two points at the middle of the surface A are fixed to avoid the rotation of the auxetic metamaterial, given in **Fig. 26** (*b*). As shown in **Fig. 26** (*c*), a displacement with 1 mm in Z direction is homogenously imposed on the surface C with the normal direction Z+ in Condition 3. It should be noted that the surfaces A and C are opposite along Z direction. The deformations of the top and bottom surfaces in X direction of the auxetic metamaterial are displayed in **Fig. 27**. In order to obtain a more accurate value, the difference of the average displacements on the top and bottom surfaces is viewed as the deformation degree of auxetic metamaterial 1 in the X direction. The displacement mean on the top surface is equal to 0.0239 mm, and the mean on the bottom surface is -0.0227 mm. Hence, the deformation of auxetic metamaterial in X direction is equal to $\Delta x = 0.0466\text{mm}$. The negative Poisson's ratio is defined by $\nu = -\Delta x/\Delta z = -0.0466$. We also consider different displacements imposed on the Surface C, ranging from 0.1mm to 1mm, and the corresponding negative Poisson's ratios in different cases are all equal to -0.0466, shown in **Fig. 28**. The simulated values are mostly identical to the result calculated by the homogenization in **Table 3**.

Finally, all the 3D printing prototypes for the topologically-optimized 3D auxetic microstructures No. 1 to 6 are fabricated using the SLS technique, shown in **Fig. 29**, respectively.

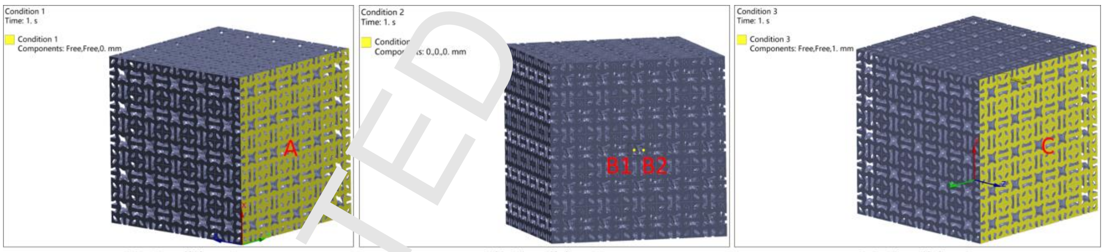

(*a*) Condition 1 (*b*) Condition 2 (*c*) Condition 3

Fig. 26 Boundary conditions imposed on the auxetic metamaterial

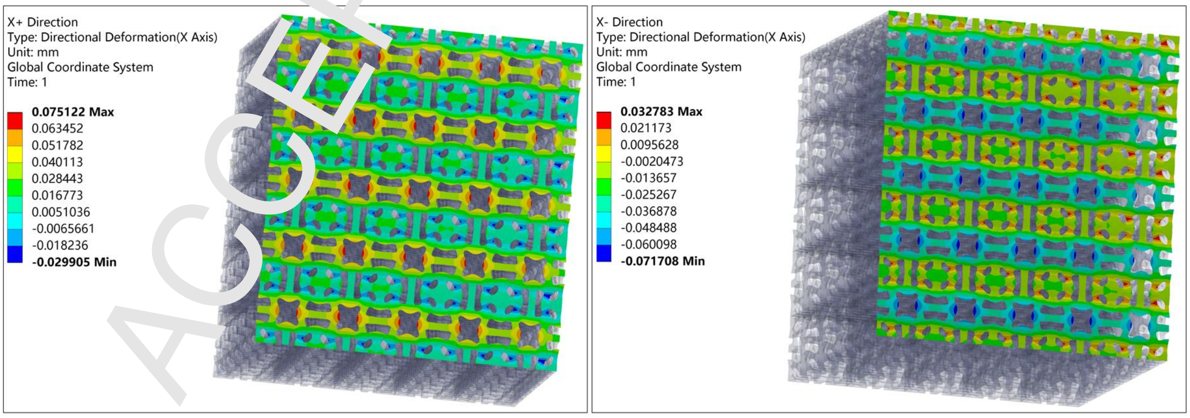

(*a*) Displacements of the top surface (*b*) Displacements of the bottom surface

Fig. 27. Displacement responses of auxetic metamaterial

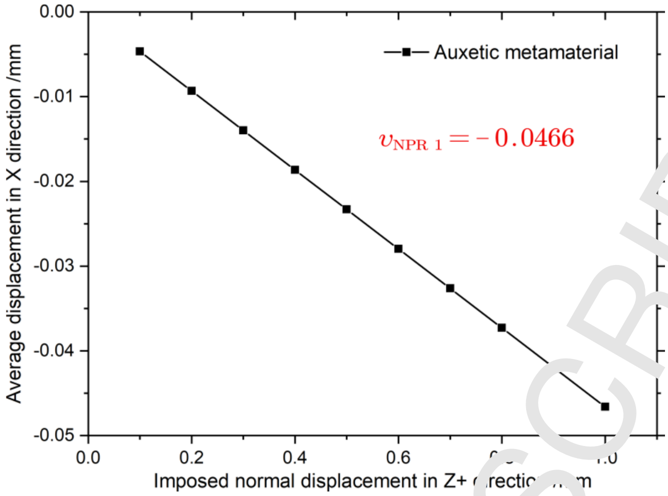

Fig. 28. Mechanical responses of auxetic metamaterial

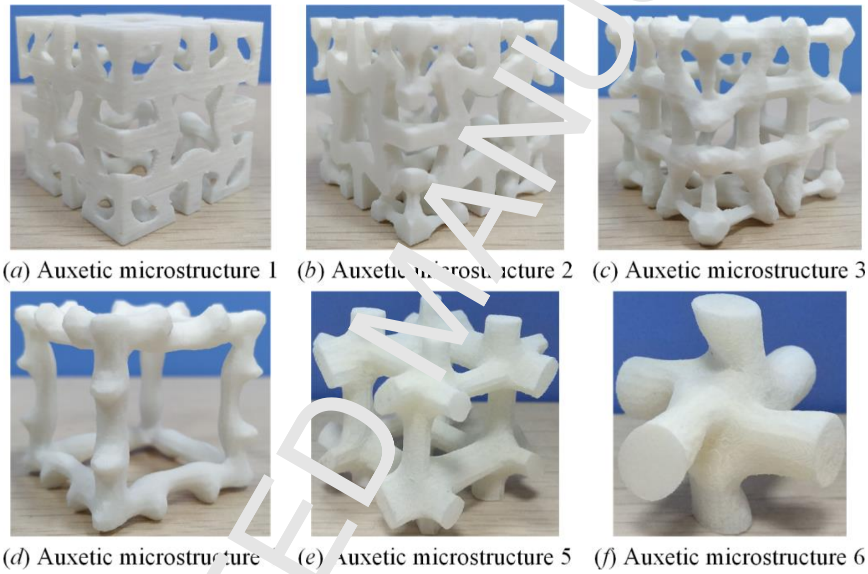

Fig. 29. 3D printing samples for six auxetic microstructures.

7 Conclusions

In this paper, we present an effective and efficient ITO method for the optimization of 2D and 3D auxetic metamaterials, where a sufficiently smooth and continuous DDF is constructed to represent the structural topology and IGA is applied to solve the displacement responses in microstructures. The homogenization to predict the macroscopic effective properties is numerical implemented by the IGA, with the consideration of the periodic boundary conditions. A relaxed form of the OC method is applied to derive the advancing of the structural topology.

In numerical examples, 2D and 3D auxetic microstructures are studied to demonstrate the effectiveness and efficiency of the ITO method. As we can see, the key characteristic of the current method is to optimize the DDF for material microstructures with the auxetic behavior, rather than the spatial arrangements of element densities. The optimized topologies of auxetics have the smooth boundaries and distinct interfaces, which is beneficial to the latter manufacturing. Additionally, the ITO method is featured with the higher efficiency for the optimization of 3D auxetic microstructures, only 37 steps for the auxetic microstructure No.1 and 52 iterations for the auxetic microstructure No.2. A series of new and interesting auxetic microstructures can be achieved. The proposed ITO method is general, and in the future, it can be extended to other more advanced topological design problems, like the nonlinear and multifunctional material microstructures.

Acknowledgments

This work was partially supported by the Australian Research Council (ARC) - Discovery Projects [160102491], and the China Equipment Pre-research Program [41423010102], and the National Basic Scientific Research Program of China (JCKY2016110C012).

References

[1] X. Yu, J. Zhou, H. Liang, Z. Jiang, L. Wu, Mechanical metamaterials associated with stiffness, rigidity and compressibility: A brief review, Prog. Mater. Sci. 94 (2018) 114–173. doi:10.1016/j.pmatsci.2017.12.003.

[2] R. Lakes, Foam structures with a negative Poisson's ratio, Science (80-.). 235 (1987) 1038–1041.

[3] C. Huang, L. Chen, Negative Poisson's Ratio in Modern Functional Materials, Adv. Mater. 28 (2016) 8079–8096. doi:10.1002/adma.201601363.

[4] I.G. Masters, K.E. Evans, Models for the elastic deformation of honeycombs, Compos. Struct. 35 (1996) 403–422. doi:10.1016/S0263-8223(96)00054-2.

[5] C.. Smith, J.. Grima, K.. Evans, A novel mechanism for generating auxetic behaviour in reticulated foams: missing rib foam model, Acta Mater. 48 (2000) 4349–4356. doi:10.1016/S1359-6454(00)00269-X.

[6] A. Spadoni, M. Ruzzene, Elasto-static micropolar behavior of a chiral auxetic lattice, J. Mech. Phys. Solids. 60 (2012) 156–171. doi:10.1016/J.JMPS.2011.09.012.

[7] T. Frenzel, M. Kadic, M. Wegener, Three-dimensional mechanical metamaterials with a twist., Science (80-.). 358 (2017) 1072–1074. doi:10.1126/science.aao4640.

[8] J.N. Grima, K.E. Evans, Auxetic behavior from rotating squares, Springer. 19 (2000) 1563–1565. https://link.springer.com/content/pdf/10.1023/A:1006781224002.pdf (accessed November 15, 2018).

[9] X. Ren, R. Das, P. Tran, T.D. Ngo, Y.M. Xie, Auxetic metamaterials and structures: a review, Smart Mater. Struct. 27 (2018) 023001. http://stacks.iop.org/0964-1726/27/i=2/a=023001.

[10] K.K. Saxena, R. Das, E.P. Calius, Three Decades of Auxetics Research − Materials with Negative Poisson's Ratio: A Review, Adv. Eng. Mater. 18 (2016) 1847–1870. doi:10.1002/adem.201600053.

[11] J.E. Cadman, S. Zhou, Y. Chen, Q. Li, On design of multi-functional microstructural materials, J. Mater. Sci. (2013). doi:10.1007/s10853-012-6643-4.

[12] M. Osanov, J.K. Guest, Topology Optimization for Architected Materials Design, Annu. Rev. Mater. Res. 46 (2016) 211–233. doi:10.1146/annurev-matsci-070115-031826.

[13] M.P. Bendsøe, O. Sigmund, Topology Optimization: Theory, Methods and Applications, (2003).

[14] M.P. Bendsøe, N. Kikuchi, Generating optimal topologies in stuctural design using a homogenization method, Comput Methods Appl Mech Eng. 71 (1988) 197–224.

[15] M. Zhou, G.I.N. Rozvany, The COC algorithm, Part II: Topological, geometrical and generalized shape optimization, Comput. Methods Appl. Mech. Eng. 89 (1991) 309–336. doi:10.1016/0045-7825(91)90046-9.

[16] M.P. Bendsøe, O. Sigmund, Material interpolation schemes in topology optimization, Arch. Appl. Mech. 69 (1999) 635–654. doi:10.1007/s004190050248.

[17] Y.M. Xie, G.P. Steven, A simple evolutionary procedure for structural optimization, Comput. Struct. 49 (1993) 885–969.

[18] J.A. Sethian, A. Wiegmann, Structural Boundary Design via Level Set and Immersed Interface Methods, J. Comput. Phys. 163 (2000) 489–528. doi:10.1006/jcph.2000.6581.

[19] M.Y. Wang, X. Wang, D. Guo, A level set method for structural topology optimization, Comput. Methods Appl. Mech. Eng. 192 (2003) 227–246. doi:10.1016/S0045-7825(02)00559-5.

[20] G. Allaire, F. Jouve, A.M. Toader, Structural optimization using sensitivity analysis and a level-set method, J. Comput. Phys. 194 (2004) 363–393. doi:DOI 10.1016/j.jcp.2003.09.032.

[21] J.M.J. Guedes, N. Kikuchi, Preprocessing and Postprocessing for Materials Based on the Homogenization Method With Adaptive Finite Element Methods, Comput. Methods Appl. Mech. Eng. 83 (1990) 143–198. doi:10.1016/0045-7825(90)90148-F.

[22] O. Sigmund, Materials with prescribed constitutive parameters: An inverse homogenization problem, Int. J. Solids Struct. 31 (1994) 2313–2329. doi:10.1016/0020-7683(94)90154-6.

[23] J.K. Guest, J.H. Prévost, Optimizing multifunctional materials: Design of microstructures for maximized stiffness and fluid permeability, Int. J. Solids Struct. (2006). doi:10.1016/j.ijsolstr.2006.03.001.

[24] A. Clausen, F. Wang, J.S. Jensen, O. Sigmund, J.A. Lewis, Topology Optimized Architectures with Programmable Poisson's Ratio over Large Deformations, Adv. Mater. 27 (2015) 5523–5527. doi:10.1002/adma.201502485.

[25] H. Li, Z. Luo, L. Gao, P. Walker, Topology optimization for functionally graded cellular composites with metamaterials by level sets, Comput. Methods Appl. Mech. Eng. 328 (2018) 340–364. doi:10.1016/J.CMA.2017.09.008.

[26] J. Gao, Z. Luo, H. Li, P. Li, L. Gao, Dynamic multiscale topology optimization for multi-regional micro-structured cellular composites, Compos. Struct. 211 (2019) 401–417. doi:10.1016/J.COMPSTRUCT.2018.12.031.

[27] J. Gao, Z. Luo, H. Li, L. Gao, Topology optimization for multiscale design of porous composites with multi-domain microstructures, Comput. Methods Appl. Mech. Eng. 344 (2019) 451–476. doi:10.1016/J.CMA.2018.10.017.

[28] E. Andreassen, B.S. Lazarov, O. Sigmund, Design of manufacturable 3D extremal elastic microstructure, Mech. Mater. 69 (2014) 1–10. doi:https://doi.org/10.1016/j.mechmat.2013.09.018.

[29] Y. Wang, Z. Luo, N. Zhang, Z. Kang, Topological shape optimization of microstructural metamaterials using a level set method, Comput. Mater. Sci. 87 (2014) 178–186.

[30] F. Wang, O. Sigmund, J.S. Jensen, Design of materials with prescribed nonlinear properties, J. Mech. Phys. Solids. 69 (2014) 156–174. doi:https://doi.org/10.1016/j.jmps.2014.05.003.

[31] N.T. Kaminakis, G.A. Drosopoulos, G.E. Stavroulakis, Design and verification of auxetic microstructures using topology optimization and homogenization, Arch. Appl. Mech. 85 (2015) 1289–1306. doi:10.1007/s00419-014-0970-7.

[32] L. Xia, P. Breitkopf, Design of materials using topology optimization and energy-based homogenization approach in Matlab, Struct. Multidiscip. Optim. 52 (2015) 1229–1241. doi:10.1007/s00158-015-1294-0.

[33] J. Wu, Z. Luo, H. Li, N. Zhang, Level-set topology optimization for mechanical metamaterials under hybrid uncertainties, Comput. Methods Appl. Mech. Eng. 319 (2017) 414–441. doi:10.1016/J.CMA.2017.03.002.

[34] F. Wang, Systematic design of 3D auxetic lattice materials with programmable Poisson's ratio for finite strains, J. Mech. Phys. Solids. 114 (2018) 303–318. doi:10.1016/j.jmps.2018.01.013.

[35] H. Zong, H. Zhang, Y. Wang, M.Y. Wang, J.Y.H. Fuh, On two-step design of microstructure with desired Poisson's ratio for AM, Mater. Des. 159 (2018) 90–102. doi:https://doi.org/10.1016/j.matdes.2018.08.032.

[36] C.R. de Lima, G.H. Paulino, Auxetic structure design using compliant mechanisms: A topology optimization approach with polygonal finite elements, Adv. Eng. Softw. (2018). doi:10.1016/J.ADVENGSOFT.2018.12.002.

[37] T.J.R. Hughes, The finite element method: linear static and dynamic finite element analysis, Courier Corporation, 2012.

[38] T.J.R. Hughes, J.A. Cottrell, Y. Bazilevs, Isogeometric analysis: CAD, finite elements, NURBS, exact geometry and mesh refinement, Comput. Methods Appl. Mech. Eng. 194 (2005) 4135–4195. doi:10.1016/j.cma.2004.10.008.

[39] J.A. Cottrell, T.J.R. Hughes, Y. Bazilevs, Isogeometric Analysis: Toward Integration of CAD and FEA, 2009. doi:10.1002/9780470749081.

[40] V.P. Nguyen, C. Anitescu, S.P.A. Bordas, T. Rabczuk, Isogeometric analysis: An overview and computer implementation aspects, Math. Comput. Simul. 117 (2015) 89–116. doi:10.1016/J.MATCOM.2015.05.008.

[41] Y.-D. Seo, H.-J. Kim, S.-K. Youn, Isogeometric topology optimization using trimmed spline surfaces, Comput. Methods Appl. Mech. Eng. 199 (2010) 3270–3296. doi:https://doi.org/10.1016/j.cma.2010.06.033.

[42] B. Hassani, M. Khanzadi, S.M. Tavakkoli, An isogeometrical approach to structural topology optimization by optimality criteria, Struct. Multidiscip. Optim. 45 (2012) 223–233. doi:10.1007/s00158-011-0680-5.

[43] L. Dedè, M.J. Borden, T.J.R. Hughes, Isogeometric Analysis for Topology Optimization with a Phase Field Model, Arch. Comput. Methods Eng. 19 (2012) 427–465. doi:10.1007/s11831-012-9075-z.

[44] X. Qian, Topology optimization in B-spline space, Comput. Methods Appl. Mech. Eng. 265 (2013) 15–35. doi:10.1016/J.CMA.2013.06.001.

[45] Z. Luo, M.Y. Wang, L. Tong, S. Wang, Shape and topology optimization of compliant mechanisms using a parameterization level set method, J. Comput. Phys. 227 (2007) 680–705.

[46] Y. Wang, D.J. Benson, Isogeometric analysis for parameterized LSM-based structural topology optimization, Comput. Mech. 57 (2016) 19–35. doi:10.1007/s00466-015-1219-1.

[47] H.A. Jahangiry, S.M. Tavakkoli, An isogeometrical approach to structural level set topology optimization, Comput. Methods Appl. Mech. Eng. 319 (2017) 240–257. doi:https://doi.org/10.1016/j.cma.2017.02.005.

[48] H. Ghasemi, H.S. Park, T. Rabczuk, A level-set based IGA formulation for topology optimization of flexoelectric materials, Comput. Methods Appl. Mech. Eng. 313 (2017) 239–258. doi:https://doi.org/10.1016/j.cma.2016.09.029.

[49] H. Liu, D. Yang, P. Hao, X. Zhu, Isogeometric analysis based topology optimization design with global stress constraint, Comput. Methods Appl. Mech. Eng. 342 (2018) 625–652. doi:https://doi.org/10.1016/j.cma.2018.08.013.

[50] X. Xie, S. Wang, M. Xu, Y. Wang, A new isogeometric topology optimization using moving morphable components based on R-functions and collocation schemes, Comput. Methods Appl. Mech. Eng. 339 (2018) 61–90. doi:https://doi.org/10.1016/j.cma.2018.04.048.

[51] X. Guo, W. Zhang, W. Zhong, Doing Topology Optimization Explicitly and Geometrically—A New Moving Morphable Components Based Framework, J. Appl. Mech. 81 (2014) 081009. doi:10.1115/1.4027609.

[52] Q.X. Lieu, J. Lee, Multiresolution topology optimization using isogeometric analysis, Int. J. Numer. Methods Eng. 112 (2017) 2025–2047. doi:10.1002/nme.5593.

[53] Q.X. Lieu, J. Lee, A multi-resolution approach for multi-material topology optimization based on isogeometric analysis, Comput. Methods Appl. Mech. Eng. 323 (2017) 272–302. doi:10.1016/J.CMA.2017.05.009.

[54] Z.-P. Wang, L.H. Poh, J. Dirrenberger, Y. Zhu, S. Forest, Isogeometric shape optimization of smoothed petal auxetic structures via computational periodic homogenization, Comput. Methods Appl. Mech. Eng. 323 (2017) 250–271. doi:10.1016/J.CMA.2017.05.013.

[55] C. De Boor, A practical guide to splines, Springer-Verlag New York, 1978.

[56] E. Andreassen, C.S. Andreasen, How to determine composite material properties using numerical homogenization, Comput. Mater. Sci. 83 (2014) 488–495. doi:10.1016/J.COMMATSCI.2013.09.006.

[57] J. Gao, H. Li, L. Gao, M. Xiao, Topological shape optimization of 3D micro-structured materials using energy-based homogenization method, Adv. Eng. Softw. 116 (2018) 89–102. doi:10.1016/j.advengsoft.2017.12.002.

[58] K. Matsui, K. Terada, Continuous approximation of material distribution for topology optimization, Int. J. Numer. Methods Eng. 59 (2004) 1925–1944. doi:10.1002/nme.945.

[59] G.H. Paulino, C.H. Le, A modified Q4/Q4 element for topology optimization, Struct. Multidiscip. Optim. 37 (2009) 255–264. doi:10.1007/s00158-008-0228-5.

[60] Z. Kang, Y. Wang, A nodal variable method of structural topology optimization based on Shepard interpolant, Int. J. Numer. Methods Eng. 90 (2012) 329–342. doi:10.1002/nme.3321.

[61] Z. Luo, N. Zhang, Y. Wang, W. Gao, Topology optimization of structures using meshless density variable approximants, Int. J. Numer. Methods Eng. 93 (2013) 443–464. doi:10.1002/nme.4394.

[62] D. Shepard, A two-dimensional interpolation function for irregularly-spaced data, in: Proc. 1968 23rd ACM Natl. Conf. -, ACM, 1968: pp. 517–524. doi:10.1145/800186.810616.

[63] H. Wendland, Piecewise polynomial, positive definite and compactly supported radial functions of minimal degree, Adv. Comput. Math. 4 (1995) 389–396.

[64] G.I.N. Rozvany, M.P. Bendsøe, U. Kirsch, Layout optimization of structures, Appl. Mech. Rev. 48 (1995) 41–119. doi:10.1115/1.3005097.

[65] Z.-D. Ma, N. Kikuchi, H.-C. Cheng, Topological design for vibrating structures, Comput. Methods Appl. Mech. Eng. 121 (1995) 259–280. doi:10.1016/0045-7825(94)00714-X.